Uncovering circuit mechanisms of current sinks and sources with biophysical simulations of primary visual cortex

Atle E. Rimehaug[1], Alexander J. Stasik[2], Espen Hagen[2,3], Yazan N. Billeh[5], Joshua H. Siegle[5], Kael Dai[5], Shawn R. Olsen[5], Christof Koch[5], Gaute T. Einevoll[2,4], and Anton Arkhipov[5,*]

[1]Department of Informatics, University of Oslo, Oslo, Norway
[2]Department of Physics, University of Oslo, Oslo, Norway
[3]Department of Data Science, Norwegian University of Life Sciences, Ås, Norway
[4]Department of Physics, Norwegian University of Life Sciences, Ås, Norway
[5]Mindscope Program, Allen Institute, Seattle, Washington, USA

* Lead contact
Correspondence: antona@alleninstitute.org; atleeri@ifi.uio.no

Abstract

Local field potential (LFP) recordings reflect the dynamics of the current source density (CSD) in brain tissue. The synaptic, cellular and circuit contributions to current sinks and sources are ill-understood. We investigated these in mouse primary visual cortex using public Neuropixels recordings and a detailed circuit model based on simulating the Hodgkin-Huxley dynamics of numerous cortical neurons belonging to 17 cell types. The model simultaneously captured spiking and CSD responses and demonstrated a two-way dissociation: Firing rates are altered with minor effects on the CSD pattern by adjusting synaptic weights, and CSD is altered with minor effects on firing rates by adjusting synaptic placement on the dendrites. We describe how thalamocortical inputs and recurrent connections sculpt specific sinks and sources early in the visual response, whereas cortical feedback crucially alters them in later stages. Our findings show that CSD analysis provides powerful constraints for modeling beyond those from considering spikes.

Introduction

The local field potential (LFP) is the low-frequency component (below a few hundred Hertz) of the extracellular potential recorded in brain tissue that originates from the transmembrane currents in the vicinity of the recording electrode (Lindén et al., 2011; Buzsáki, Anastassiou, and Koch, 2012; Einevoll et al., 2013; Pesaran et al., 2018; Sinha and Narayanan, 2021). While the high-frequency component of the extracellular potential, the single- or multi-unit activity (MUA), primarily reflects action potentials of one or more nearby neurons, the LFP predominantly stems from currents caused by synaptic inputs (Mitzdorf, 1985; Einevoll et al., 2007) and their associated return currents through the membranes. Thus, cortical LFPs represent aspects of neural activity that are complementary to those reflected in spikes, and as such, it can provide additional information about the underlying circuit dynamics from extracellular recordings.

Applications of LFP are diverse and include investigations of sensory processing (Baumgartner and Barth, 1990; Victor et al., 1994; Kandel and Buzsáki, 1997; Henrie and Shapley, 2005; Einevoll et al., 2007; Belitski et al., 2008; Montemurro et al., 2008; Niell and Stryker, 2008; Nauhaus et al., 2008; Bastos et al., 2015; Senzai, Fernandez-Ruiz, and Buzsáki, 2019), motor planning (Scherberger, Jarvis and Andersen, 2005; Roux, Mackay and Riehle, 2006) and higher cognitive processes (Pesaran et al., 2002; Womelsdorf et al., 2005; Liu and Newsome, 2006; Kreiman et al., 2006; Liebe et al., 2012). The LFP is also a promising candidate signal for steering neuroprosthetic devices (Mehring et al., 2003; Andersen, Musallam and Pesaran, 2004; Rickert et al., 2005; Markowitz et al., 2011; Stavisky et al., 2015) and for monitoring neural activity in human recordings (Mukamel and Fried, 2012) because the LFP is more easily and stably recorded in chronic settings than spikes. Due to the vast number of neurons and multiple neural processes contributing to the LFP, however, it can be challenging to interpret (Buzsáki, Anastassiou, and Koch, 2012; Einevoll et al., 2013; Hagen et al., 2016). While we have extensive phenomenological understanding of the LFP, less is known about how different cell and synapse types and connection patterns contribute to the LFP or how these contributions are sculpted by different information processing streams (e.g., feedforward vs. feedback) or brain state.

One way to improve its interpretability is to calculate the current source density (CSD) from the LFP, which is a more localized measure of activity, and easier to read in terms of the underlying neural processes. The current sinks and sources indicate where positive ions flow into and out of cells, respectively, and are constrained by Kirchoff's current law (i.e., currents

sum to zero over the total membrane area of a neuron). However, the interpretation of current sinks and sources is inherently ambiguous, as several processes can be the origin of a current sink or source (Buzsáki, 2006; Pettersen et al., 2006; Einevoll et al., 2007). For example, a current source may reflect an inhibitory synaptic current or an outflowing return current resulting from excitatory synaptic input elsewhere on the neuron, and there is no simple way of knowing which it is from an extracellular recording alone (Buzsáki, 2006).

Another approach to uncovering the biophysical origins of current sinks and sources, and by extension the LFP, is to simulate them computationally (Pettersen, Hagen, and Einevoll, 2008; Einevoll et al., 2013). Following the classic work by Rall in the 1960s (Rall, 1962), a forward-modeling scheme in which extracellular potentials are calculated from neuron models with detailed morphologies using volume conduction theory under the line source approximation has been established (Holt and Koch, 1999). With this framework, we have achieved a good understanding of the biophysical origins of extracellular potentials in single cells, both spikes (Koch, 1999; Pettersen and Einevoll, 2008; Hay et al., 2011) and LFPs (Lindén et al, 2010). Expanding on this understanding, models composed of populations of unconnected neurons (e.g. Pettersen, Hagen, and Einevoll, 2008; Lindén et al., 2011; Schomburg et al., 2012; Łęski et al., 2013; Sinha and Naryanan, 2015; Hagen et al., 2017; Ness et al., 2018) and recurrent network models (e.g. Vierling-Claassen et al., 2010; Reimann et al., 2013; Głąbska et al., 2014; Tomsett et al., 2015; Hagen et al., 2016; Hagen et al., 2018; Chatzikalymniou and Skinner, 2018) have been used to study the neural processes underlying LFP.

While interesting insights about CSD and LFP were obtained from these computational approaches, establishing a direct relationship between the biological details of the circuit structure and the electrical signal like LFP remains a major unresolved challenge. One reason is that the amount and quality of data available for modeling the circuit architecture in detail has been limited. This situation improved substantially in recent years, and a broad range of data on the composition, connectivity, and physiology of cortical circuits have been integrated systematically (Billeh et al., 2020) in a biophysically detailed model of mouse primary visual cortex (area V1). In addition, significant improvements were achieved in the area of experimental recordings of the LFP and the simultaneous spiking responses. In particular, the Neuropixels probes (Jun et al., 2017) have recently allowed for recordings of LFP and hundreds of units across the cortical depth in multiple areas, with 20 μm spacing between recording channels allowing for an unprecedented level of spatial detail. These developments provide unique opportunities to improve our understanding of circuit mechanisms that determine LFP patterns.

Here, we analyze spikes and LFP from the publicly available visual coding dataset recorded using Neuropixels probes (www.brain-map.org; Siegle et al., 2021), and seek to explain these using the mouse V1 model developed by Billeh et al. (2020). The model is comprised of more than 50,000 biophysically detailed neuron models surrounded by an annulus of almost 180,000 generalized leaky-integrate-and-fire units. The neuron models belong to 17 different cell type classes: one inhibitory class (Htr3a) in layer 1, and four classes in each of the other layers (2/3, 4, 5, and 6) where one is excitatory and three are inhibitory (Pvalb, Sst, Htr3a) in each layer. The visual coding dataset consists of simultaneous recordings from six Neuropixels 1.0 probes across a range of cortical and subcortical structures in 58 mice while they are exposed to a range of visual stimuli (about 100,000 units and 2 billion spikes over two hours of recording).

In our analysis of this dataset, we identified a canonical CSD pattern that captures the evoked response in mouse V1 to a full-field flash. We then modified the biophysically detailed model of mouse V1 to reproduce the canonical CSD pattern. In this process, we discovered that the model can be modified by adjusting the synaptic weights to reproduce the experimental firing rates with only minor effects on the simulated CSD, and, conversely, that the simulated CSD can be altered with only minor effects on the firing rates by adjusting synaptic placement. Furthermore, we found that comparing the simulated CSD to the experimental CSD revealed discrepancies between model and data that were not apparent from only comparing the firing rates. Additionally, it was not until feedback from higher cortical visual areas (HVAs) was added to the model that simulations reproduced both the experimentally recorded CSD and firing rates, as opposed to only the firing rates.
This bio-realistic modeling approach sheds light on specific components of the V1 circuit that contribute to the generation of the major sinks and sources of the CSD in response to abrupt visual stimulation. Our findings demonstrate that utilizing the LFP and/or the CSD in modeling can aid model configuration and implementation by revealing discrepancies between models and experiments and provide additional constraints on model parameters beyond those offered by the spiking activity. The new model obtained here is provided freely (https://www.dropbox.com/sh/x6zuogmjx8zns9f/AAAQbQbdXABsbbHUhC-qGBP7a?dl=0) to the community to facilitate further applications of biologically detailed modeling.

Results

Spikes and LFP were recorded across multiple brain areas, with a focus on six cortical (V1, LM, AL, RL, AM, PM) and two thalamic (LGN, LP) visual areas, using Neuropixels probes in 58 mice (Siegle et al., 2021).

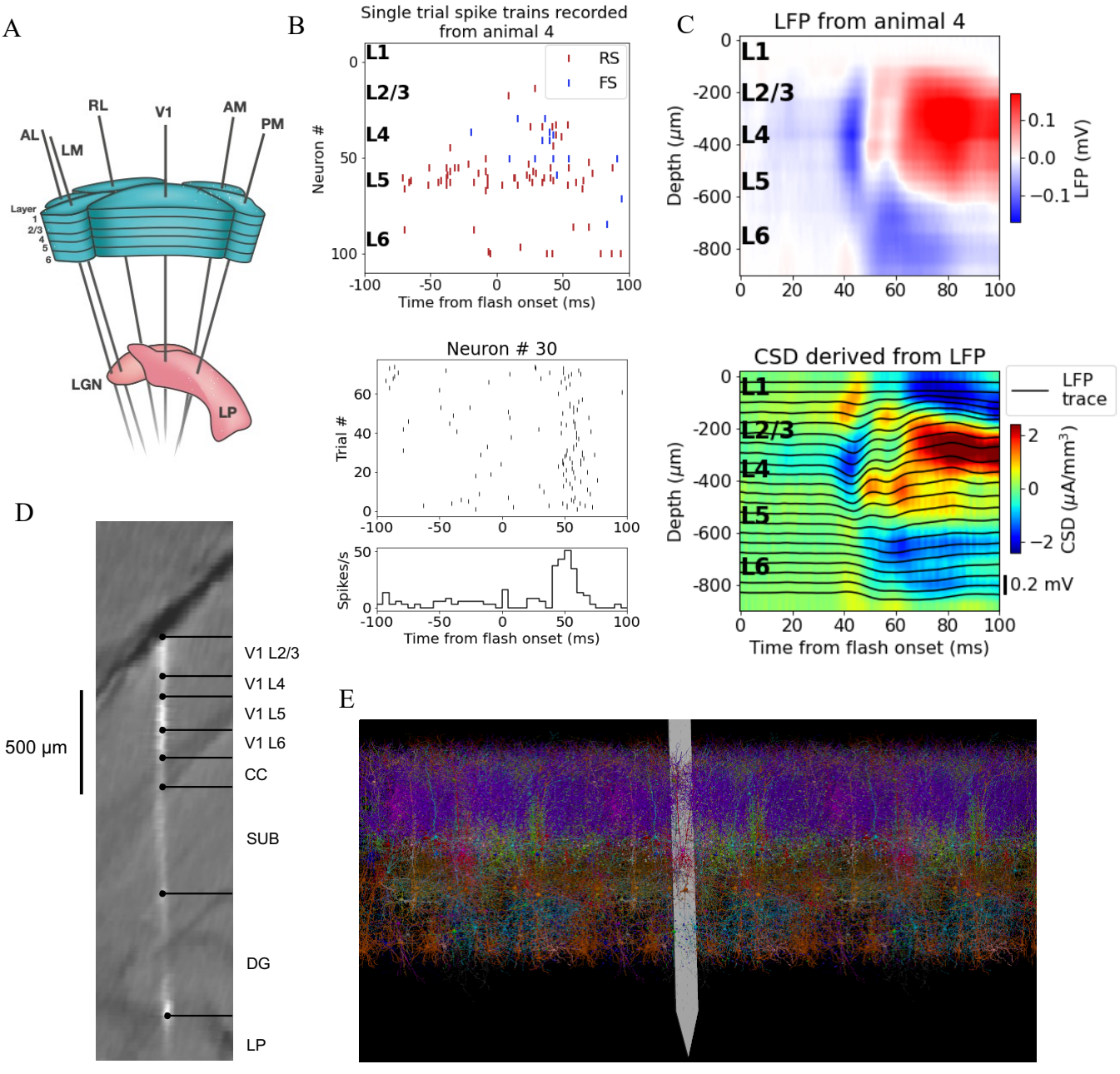

Figure 1: Illustration of experimental data and the biophysical model for mouse primary visual cortex (V1). (A) Schematic of the experimental setup, with six Neuropixels probes inserted into six cortical (V1, LM, RL, AL, PM, AM) and two thalamic areas (LGN, LP). **(B)** Top: Spikes from many simultaneously recorded neurons in V1 during a single trial. Bottom: Spikes from a single neuron

recorded across multiple trials. In both cases, the stimulus was a full-field bright flash (onset at time 0, offset at 250 ms). **(C)** Top: LFP across all layers of V1 in response to the full-field bright flash, averaged over 75 trials in a single animal. Bottom: CSD computed from the LFP with the delta iCSD method. **(D)** Histology displaying trace of the Neuropixels probe across layers in V1, subiculum (SUB) and dentate gyrus (DG). **(E)** Visualization of the V1 model with the Neuropixels probe *in situ*.

A schematic of the six probes used to perform the recordings in individual mice is shown in Fig. 1A, and the spikes and LFP recorded in V1 of an exemplar mouse during presentation of a full-field bright flash stimulus are displayed in Fig. 1B, C. The current source density (CSD) can be estimated from the LFP (averaged over 75 trials) using the delta iCSD method to obtain a more localized measure of inflowing (sinks) and outflowing currents (sources) (Pettersen et al. 2006; Einevoll et al., 2013). The biophysically detailed model of mouse V1 used to simulate the neural activity and the recorded potential in response to the full-field flash stimulus is illustrated in Fig. 1E. The extracellular electric field in the model was recorded on an array of simulated point electrodes (Dai et al., 2020) arranged in a straight line (Fig. 1D) and separated by *20 μm*, consistent with Neuropixels probes, shown in Fig. 1E to scale with the model.

Uncovering a canonical visually evoked CSD response

We first established a “typical” experimentally recorded CSD pattern, to be reproduced with the model. Though there is substantial inter-trial and inter-animal variability in the evoked CSD response, we find that most trials and animals have several salient features in common. In Fig. 2A, the trial-averaged evoked CSDs from five individual mice are displayed. In the first four animals (# 1-4), we observe an early transient sink arising in layer 4 (L4) around 40 ms after flash onset, followed by a sustained source starting at about 60 ms which covers L4 and parts of layers 2/3 (L2/3) and layer 5 (L5). We also observe a sustained sink covering layers 5 and 6 (L6) emerging at around 50 ms, as well as a sustained sink covering layers 1 and 2/3 from about 60 ms. An animal that does not fully exhibit what we term the “canonical” pattern is shown in the rightmost plot (# 5 in Fig. 2A); it has an early L4 sink arising at 40 ms, but this sink is not followed by the sustained sinks and sources from 50-60 ms and onwards observed in the other animals. The timing and location of sinks and sources are, overall, similar to those described earlier by Niell & Stryker (2008), and Senzai, Fernandez-Ruiz, and Buzsáki (2019).

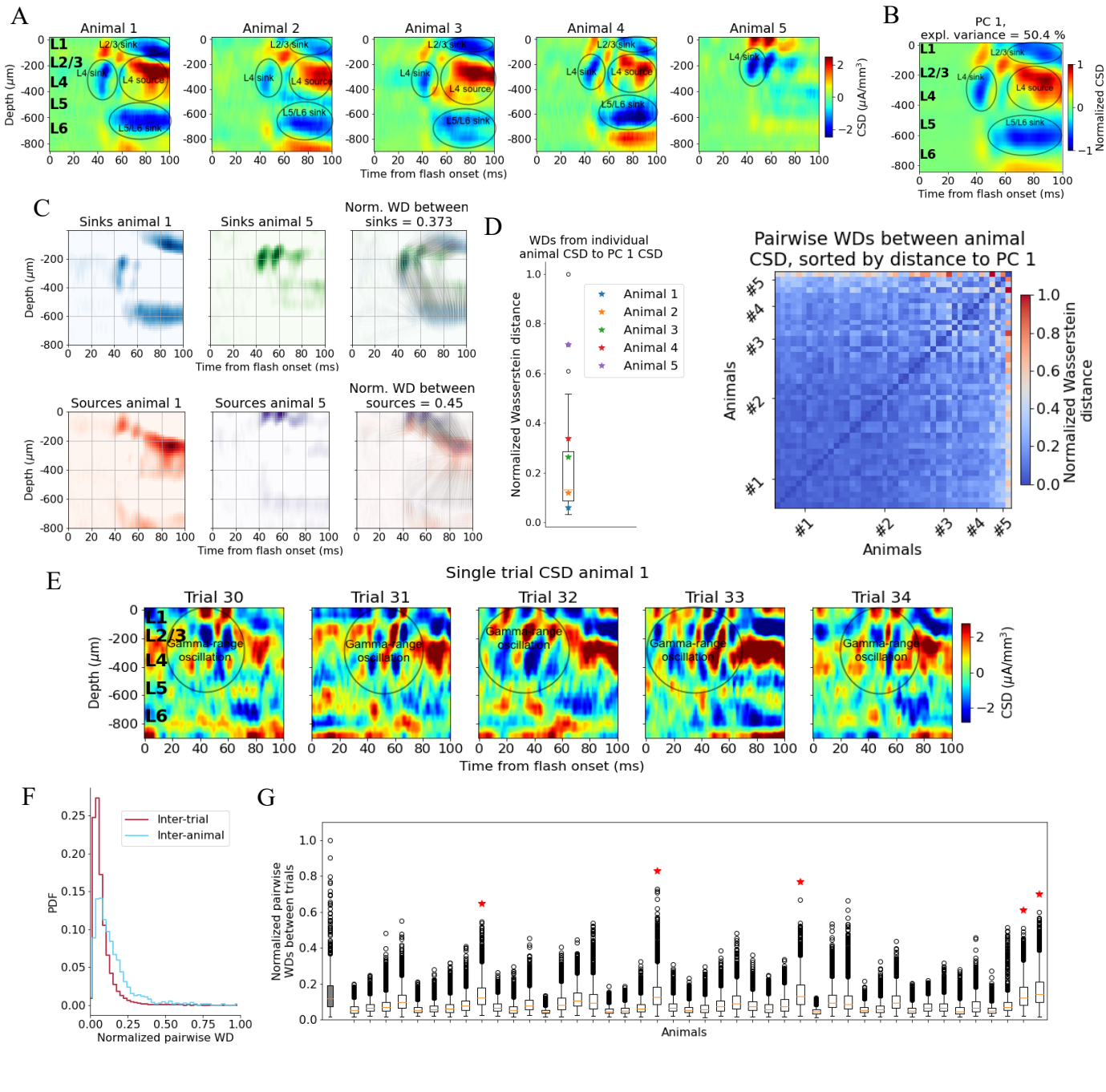

Figure 2: Variability in experimentally recorded CSD. (A) Evoked CSD response to a full-field flash averaged over 75 trials, from five animals in the dataset. **(B)** The first principal component (PC) computed from the CSD of all n=44 animals, explaining 50.4% of the variance. **(C)** Illustration of movement of sinks and sources in the calculation of the Wasserstein distance (WD) between the CSD of two animals in the dataset. The gray lines in the rightmost panels display how the sinks or sources of one animal are moved to match the distribution of sinks or sources of the other animal. **(D)** Left: WDs from each animal to the PC 1 CSD. Right: Pairwise WDs between all 44 animals sorted by their distance to the first PC**. (E)** CSD from five individual trials in example animal 1. **(F)** Distribution of pairwise distances between single trial CSD (red) and pairwise distances between trial averaged CSD of individual animals (blue). Both are normalized to the maximum pairwise distance between the trial

averaged CSD of individual animals. **(G)** Pairwise WDs between trials in each of 44 animals (white boxplots), normalized to maximal pairwise WDs between trial averaged CSD of animals. Grey-colored boxplot shows the distribution of pairwise WDs between trial-averaged CSD of individual animals, and the red stars indicate the n=5 animals for which the inter-trial variability was greater than the inter-animal variability (assessed with KS-tests, see S2 in Supplementary Figures).

To identify the robust features across animals in this dataset, we performed Principal Component Analysis (PCA) on the trial-averaged evoked CSD from all animals. Five out of the 58 animals in the data set did not have readable recordings of LFP in V1 during the presentation of the full-field flash stimuli, and the exact probe locations in V1 could not be recovered for nine other animals due to fading of fluorescent dye or artifacts in the optical projection tomography (OPT) volume (see Methods). The remaining 44 (out of the 58) animals in the data set were retained for the CSD analysis. The first principal component (PC 1) (Fig. 2B) constitutes a weighted average of the CSD patterns from all 44 animals and explains half (50.4 %) of the variance. The salient features typically observed in individual animals are also prominent in the PC 1 CSD pattern (Fig. 2B), *i.e.*, the canonical pattern.

Quantifying CSD pattern similarity

We use the Wasserstein or Earth Mover's distance (WD), to quantify the differences in CSD patterns (see Methods). The WD reflects the cost of transforming one distribution into another by moving its "distribution mass" around (Rubner et al., 1998; Arjovsky et al., 2017). An often-used analogy refers to the two distributions as two piles of dirt, where the WD tells us the minimal amount of work that must be done to move the mass of one pile around until its distribution matches the other pile (Rubner et al., 1998). In the context of CSD patterns, the WD reflects the cost of transforming the distribution of sinks and sources in one CSD pattern into the distribution of sinks and sources in another pattern, with larger WD indicating greater dissimilarity between CSD patterns. The WDs are computed between the sinks of two CSD patterns and between the sources of two CSD patterns independently, and then summed to form a total WD between the CSD patterns (Fig. 2C). The sum of all sinks and the sum of all sources in each CSD pattern are normalized to -1 and +1, respectively, so the WD only reflects differences in patterns, and not differences in the overall amplitude. The WD scales linearly with shifts in space and time.

When computing the WDs between the evoked CSD patterns of individual animals and the canonical pattern, we find that the animals with CSD patterns that, by visual inspection, resemble the canonical pattern (Fig. 2A, animals 1-4), are indeed among animals with

smaller WD, while the animal with the more distinct CSD pattern (Fig. 2A, animal 5) is an outlier (Fig. 2D).

The onset of the evoked response is less conspicuous in the single-trial CSD, due to pronounced, ongoing sinks and sources, but there is still a visible increase in magnitude from 40-50 ms and onwards (Fig. 2E), compatible with the latency of spiking responses to full-field flashes in V1 (Siegle et al., 2021). An oscillation of sinks and sources with a periodicity of ~20 ms, *i.e.*, in the gamma range is apparent in the region stretching from L2/3 to the top of L5, which appears to be either partially interrupted or drowned out by more sustained sinks and sources emerging at about 60 ms. At least some of this gamma-range activity derives from the visual flash that covers the entire visual field and that drives retinal neurons and post-synaptic targets in the lateral geniculate nucleus (LGN) in an oscillatory manner (see the pronounced gamma-range oscillation in the LGN firing rate in Fig. 3D).

The inter-trial variability is roughly comparable to the inter-animal variability of the trial-averaged responses. By computing the pairwise Wasserstein distances between single trial CSDs within each animal, and comparing it to the pairwise WD between the trial-averaged CSD of each animal, we find that inter-trial variability in CSD is significantly lower than the inter-animal variability in trial-averaged CSD (Kolmogorov-Smirnov distance = 0.33; $p < 0.001$) (Fig. 2F).

The majority of animals (39 out of 44) have a WD to the 1st principal component, PC 1, of the CSD that is less than half of the greatest WD between the CSD of individual animals and the PC 1 CSD (Fig 2D); the pairwise WDs between animals are also less than half of the maximum pairwise WD for most animals (921 out of the total 946 pairwise WDs; Fig 2E). This supports the view that most animals exhibit the canonical CSD pattern captured by the PC 1 CSD (Fig. 2B). The total inter-trial variability is smaller than the inter-animal variability, both estimated by pairwise WDs (Fig. 2F-G), though there are n=5 animals for which the inter-trial WDs are larger than the inter-animal WDs (Fig. 2G, marked by red stars; determined with KS-tests on the distribution of pairwise WDs between animals and pairwise WDs between trials in each animal - see Fig. S4).

Quantifying firing rate variability

For the spike analysis (see Methods), we distinguish between fast-spiking (FS; putative Pvalb inhibitory) neurons, and regular-spiking (RS; putative excitatory and non-Pvalb inhibitory) neurons. All FS-neurons are grouped together into one population across all

layers, while the RS-neurons are divided into separate populations for each layer (Fig. 3A). The FS-neurons are merged across layers because we set a criterion of at least 10 recorded neurons in any one layer when comparing the population firing rate in individual animals to the average population firing rate in all animals, and only *one* animal had 10 FS-neurons or more in any layer (Fig. S3). This criterion was set to have a more reliable estimate of the population firing rates in individual animals.

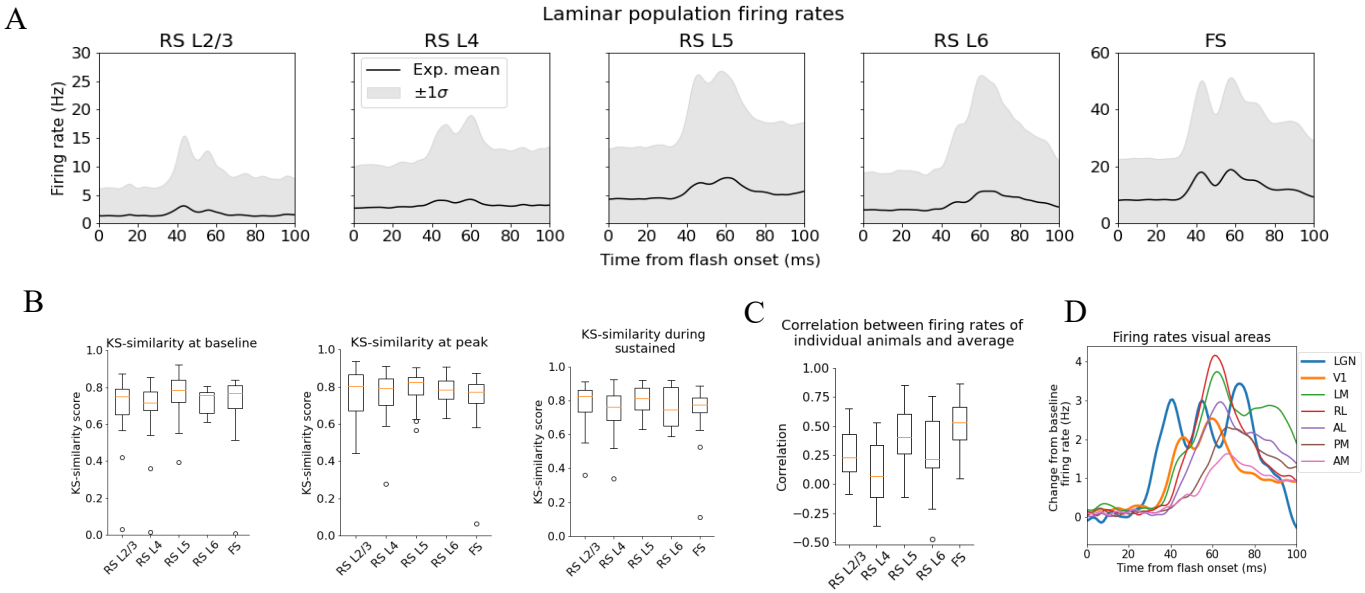

E

Period	Baseline					Peak					Sustained				
Population	**L2/3**	**L4**	**L5**	**L6**	**FS**	**L2/3**	**L4**	**L5**	**L6**	**FS**	**L2/3**	**L4**	**L5**	**L6**	**FS**
Firing rate (μ ± σ Hz)	1.2±2.5	2.6±4.3	3.2±5.0	2.4±3.9	7.9±10.1	2.4±7.1	3.8±8.8	6.6±12.7	3.6±9.2	15.9±21.5	2.4±7.1	3.8±8.8	6.6±12.7	3.6±9.2	15.9±21.5

Figure 3: Variability in experimentally recorded spikes. (A) Trial-averaged laminar population firing rates of regular-spiking (RS) cells, differentiated by layer, and fast-spiking (FS) cells across all layers in response to full-field flash. Black line: Average across all animals. Gray shaded area: ± 1 standard deviation. **(B)** Kolmogorov-Smirnov (KS) similarities (see Methods) between the trial-averaged firing rates of each individual animal and the average firing rate over cells from all animals (black line in (A)) at baseline (the interval of 250 ms before flash onset), peak evoked response (from 35 to 60 ms after flash onset), and during the sustained period (from 60 to 100 ms). **(C)** Correlations between trial-averaged firing rates of individual mice and all mice (0-100 ms after flash onset). **(D)** Baseline-subtracted evoked firing rates for excitatory cells in seven visual areas (average over trials, neurons, and mice). Note the strong, stimulus triggered gamma-range oscillations in the firing of LGN neurons (blue). **(E)** Mean (μ) ± standard deviation (σ) of population firing rates during baseline, peak evoked response, and the sustained period. Averaged across trials, neurons and time windows defined above.

We use the Kolmogorov-Smirnov (KS) similarity (defined as one minus the KS distance, see Methods) and correlation to quantify the variability in spikes. The KS-similarity gives the similarity between the distributions of average firing rates across neurons in two populations in selected time windows, with KS-similarity = 1 implying identity. As such, KS-similarity provides a metric to compare the magnitudes of firing rates in certain time periods. We defined the 'baseline' window as the period over 250 ms before the flash onset, the 'initial peak' window as 35 ms to 60 ms after flash onset, and the 'sustained' window as 60 ms to 100 ms after flash onset. The KS-similarity score during baseline is denoted "KSS_b", during the 'initial peak' "KSS_p", and 'sustained' "KSS_s". The correlation, on the other hand, is computed between two population firing rates throughout the 100 ms window. The correlation thus gives us a measure of the similarity in the temporal profile of firing rates in this interval, independent of magnitudes. We establish the experimental variability in KS-similarities and correlation by computing these metrics between the population firing rates of each individual animal and the average population firing rates of all other animals (averaged over trials for both the individual animals and the average over all other animals) (Fig. 3B-C).

The population firing rates for FS neurons are more than twice as high than RS cells during baseline, peak and sustained. Among the RS populations, the firing rate in L5 is the highest at the peak and baseline, followed by L4 and L6, while L2/3 has the lowest firing rates (Fig. 3E).

Discrepancy between the original model and experimental observations

We simulated the response to a full-field flash stimulus with the biophysical network model of mouse primary visual cortex as presented in Billeh et al., 2020. As input to the model, we used experimentally recorded LGN spike trains (Fig. 4C) (see Methods). A Poisson source, firing at a constant rate of 1 kHz, provides additional synaptic input to all cells, representing the influence from the rest of the brain ("background" input). The thalamocortical input consists of spike trains from 17,400 LGN units (Arkhipov et al., 2018; Billeh et al., 2020). The public Neuropixels data contain recordings from 1,263 regular-spiking LGN neurons across 32 mice during 75 trials of full-field bright flash presentations, resulting in 94,725 spike trains. To construct the input for each of our 10 simulation trials, we randomly sampled 10 unique subsets of spike trains from this pool, until all 17,400 units had been assigned a spike train in each trial.

Fig. 4A-B displays the resulting spiking pattern across all layers with its associated LFP. The inferred CSD exhibits a strong sink in the L5 and L6 region, matched by a strong source

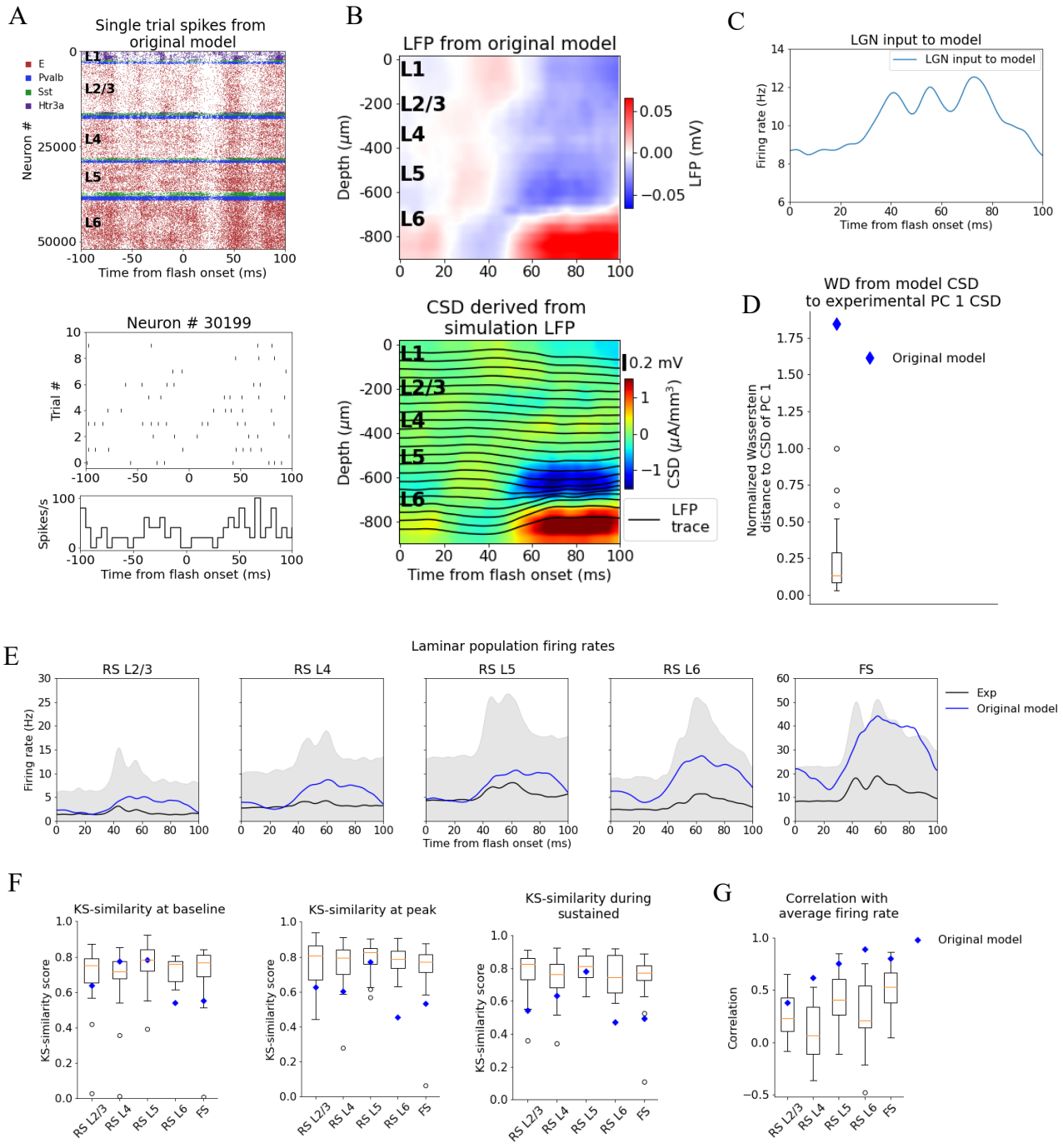

H

Period	Baseline					Peak					Sustained				
Population	**L2/3**	**L4**	**L5**	**L6**	**FS**	**L2/3**	**L4**	**L5**	**L6**	**FS**	**L2/3**	**L4**	**L5**	**L6**	**FS**
Firing rate (μ ± σ Hz)	2.2±2.8	3.8±5.0	4.8±6.0	6.1±4.9	20.4±15.3	4.1±5.7	6.7±8.8	8.3±11.2	9.9±10.0	35.8±25.6	3.9±5.7	6.9±10.5	9.5±11.2	11.4±11.1	36.7±25.8

Figure 4: LFP, CSD and spikes from simulations with the original model. (A) Top: Raster plot of all ~50,000 cells in the model's 400 μm-radius "core" region spanning all layers, in a simulation of a single trial with the flash stimulus. Bottom: Raster plot and histogram of spikes from 10 trials for an

example cell. **(B)** Top: simulated LFP averaged over 10 trials of flash stimulus. Bottom: CSD calculated from the LFP via the delta iCSD method. **(C)** Firing rate of experimentally recorded LGN spike trains used as input to the model. **(D)** Wasserstein distance between CSD from the original model (blue diamond) and PC 1 CSD from experiments together with the Wasserstein distances from experimental CSD in every animal to PC 1 CSD (boxplot), normalized to maximal distance for animals. **(E)** Experimentally recorded firing rates (black) and simulated firing rates (blue). **(F)** KS-similarity between firing rates in original model (blue diamond) or individual animals (boxplots) and firing rates in experiments at baseline, peak evoked response, and during the sustained period (defined in Fig. 3). **(G)** Correlation between firing rates of model (blue diamond) or individual animals in experiments (boxplots) and average population firing rates in experiments (0-100 ms). **(H)** Mean (μ) ± standard deviation (σ) of model firing rates during baseline, peak evoked response, and the sustained period. Averaged across trials, neurons and time windows defined above.

below it, both starting at ~50 ms after flash onset (Fig. 4B; bottom). However, the early L4 sink, the later sustained L4 source, and the sustained L2/3 sink typically observed in the experimental CSD (Fig. 2A, B) are either absent or too weak compared to the sink and source in L5 and L6. The WD from the simulated CSD to the experimental PC 1 CSD is greater than the WD between the CSD of the farthest outlier animal and the PC 1 CSD (WD = 1.84, normalized to the largest WD between CSD of individual animals and PC 1 CSD). Thus, using experimental variability as a reference, the CSD from this simulation is an outlier (Fig. 4C).

The population firing rates of the model, the KS similarities and correlation between the model and the data, are plotted together with the data in Fig. 4D-F. The magnitudes of the model firing rates are higher than the experimental firing rates in all populations and time windows (Fig. 4H). However, the KS similarities between the model firing rates and the experimental firing rates are still within the minimum to maximum range of the boxplots for the RS L2/3, RS L4, and RS L5 cells in all time windows (Fig. 4F), and during baseline for the FS cells. For RS L6 neurons the KS similarities were among the outliers of the experiments in all time windows, while for FS neurons they were among the outliers during the peak and sustained windows (RS L2/3: KSS_b = 0.62, KSS_p = 0.63, and KSS_s = 0.54; RS L4: KSS_b = 0.77, KSS_p = 0.60, and KSS_s = 0.63; RS L5 KSS_b = 0.77, KSS_p = 0.77, and KSS_s = 0.78; RS L6: KSS_b = 0.54, KSS_p = 0.45, and KSS_s = 0.47; FS: KSS_b = 0.54, KSS_p = 0.53, and KSS_s = 0.49). The temporal profile of the model firing rates are above the minimum of the boxplots for all populations (RS L2/3: r = 0.38***, RS L4: r = 0.62***, RS L5: r = 0.75***, RS L6: r = 0.90***, FS: r = 0.80***; *** p<0.001).

The original model studied in Fig. 4 produced firing rates and orientation and direction tuning consistent with recordings *in vivo* (Billeh et al., 2020), but with some shortcomings, such as relatively slow responses of V1 to the onset of visual stimuli (Arkhipov et al., 2018; Billeh et al., 2020). Here, we see even more inconsistencies reflected clearly in the CSD pattern. This demonstrates the importance of multi-modal characterization of such biologically detailed models. To investigate the properties of the cortical circuit that sculpt the CSD, we manipulated the model and observed how both the CSD and firing rate responses were improved to match the experimental data.

Adjusting the model to fit experimental firing rates

Due to the discrepancy between the magnitudes of the model firing rates and the experimental firing rates, especially with respect to the RS L6 and FS neurons, where the model firing rates were among the experimental outliers, we selectively adjusted the recurrent synaptic weights. We left the synaptic weights between LGN and the V1 model unchanged since they were well constrained by data (Billeh et al. 2020).

We first reduced the synaptic weights from all excitatory populations to the fast-spiking PV- neurons by 30% to bring their firing rates closer to the average firing rate in this population in the experiments. This resulted in increased firing rates in all other (RS) populations due to the reduced activity of the inhibitory Pvalb-neurons (Fig. S6). Therefore, we further applied reductions in the synaptic weights from all excitatory neurons to RS neurons or increases in the synaptic weights from inhibitory neurons to the RS neurons to bring their firing rates closer to the experimental average firing rates. We multiplied the recurrent synaptic weights with factors in the [0.2, 2.5] range until we arrived at a set of weights where none of the model firing rates were among the experimental outliers in any time window (KSS_b = 0.73, KSS_p = 0.77, and KSS_s = 0.70; average across RS populations and the FS population) and temporal profiles (RS L2/3: r = 0.49***, RS L4: r = 0.63***, RS L5: r = 0.71***, RS L6: r = 0.87***, FS: r = 0.86***; *** p<0.001) (Fig. 5A-C).

The resulting spatial pattern (but not the magnitude) of the CSD, however, was largely unchanged (Fig. 5D) compared to the original CSD (Fig. 4B). The overall magnitude was reduced, and there were some traces of a sink arising at 40 ms after flash onset, and a L2/3 (and L1) sink after 60 ms, but they were substantially weaker relative to the L5/L6 dipole than they were in the experiments. Furthermore, the large and sustained L4 source after 60 ms was still either absent or too weak to be visible. The WD between the CSD from this

version of the model and the experimental PC 1 CSD remained among the outliers of the animals (Fig. 5E) (Normalized WD = 1.26).

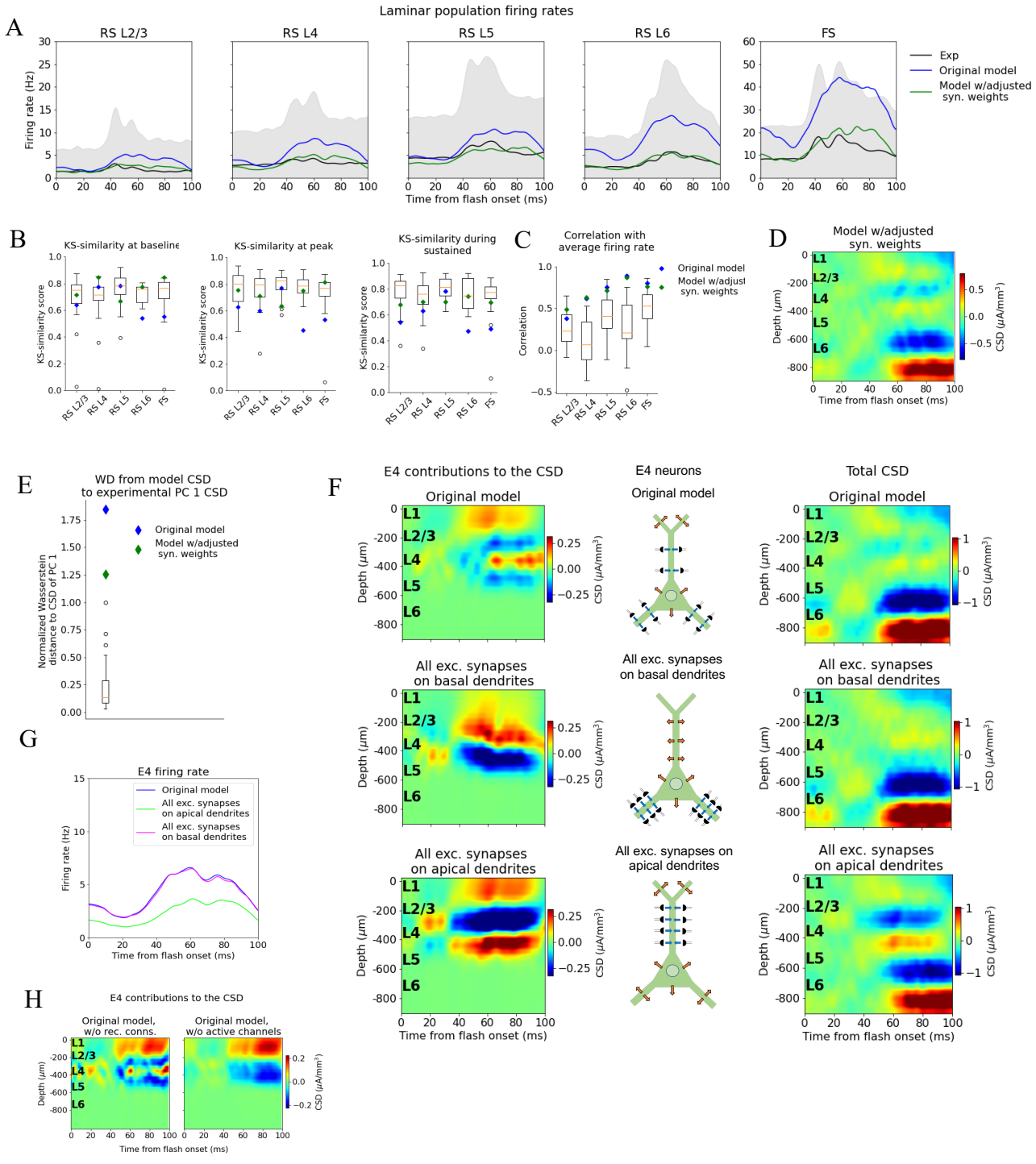

Figure 5: Adjusting the model to fit spikes or CSD. (A) Average experimentally (black) and simulated firing rates of experiments in the model with adjusted recurrent synaptic weights (green) and original model (blue). Synaptic adjustments included scaling the weights from all excitatory populations to the PV cells down by 30 % to reduce the firing rates in these fast-spiking populations, reducing the synaptic weights from excitatory populations to all others and increasing synaptic

weights from all PV cells to all other populations to compensate for the reduced inhibition. **(B)** KS similarity between firing rates of model versions (markers) or individual animals in experiments (boxplots) and firing rates of experiments at baseline, peak evoked response, and during the sustained (defined in Fig. 3**). (C)** Correlation between simulated firing rates or individual animals (boxplots) and measured firing rates (0-100 ms). **(D)** CSD resulting from simulation on model with adjusted recurrent synaptic weights. **(E**) Wasserstein distance between CSD from model versions and PC 1 CSD from experiments together with Wasserstein distances from CSD in animals to PC 1 CSD (boxplot). **(F)** Effect of different patterns of placing excitatory synapses onto layer 4 excitatory cells on this population's contribution to the simulated CSD (left) and to the total simulated CSD (right). These synaptic placement schemes with accompanying inflowing (blue arrows) and outflowing (orange arrows) currents are illustrated in the middle. **(G)** Effect of synaptic placement on the simulated population firing rate. **(H)** Contribution of L4 excitatory cells to the simulated CSD in the model where all recurrent connections have been cut (left) and when all active channels have been removed from all cells in the model (right).

Two-way dissociation between spikes and CSD

Simulations demonstrate that the LFP, and the associated CSD, can be significantly altered by changes to synaptic placement (Einevoll et al., 2007; Pettersen, Hagen, and Einevoll, 2008; Lindén et al, 2010; Lindén et al, 2011; Łęski et al., 2013; Hagen et al., 2017; Ness et al., 2018). As observed in Fig. 5A, D, adjustments of synaptic weights can modify the population firing rates substantially, yet without substantially changing the pattern of the CSD, *i.e.*, the placement and timing of sinks and sources. The inverse can also occur; that is, the CSD pattern can be altered extensively with only minor effects on firing rates (Fig. 5F-G).

In the model's original network configuration, L4 excitatory neurons received geniculate input from synapses placed within 150 μm from the soma on both basal and apical dendrites, and excitatory, recurrent input from other V1 neurons within 200 μm from the soma on both basal and apical dendrites. We tested the effects of synaptic location by placing all synapses from both LGN and excitatory neurons onto the basal dendrites of L4 excitatory neurons (within the same ranges as in the original configuration). This increased the contribution from the L4 excitatory neurons to the total CSD (Fig 5F, middle row, leftmost plot) by a factor of ~2, and led to a dipole pattern with a single sink at the bottom and a single source at the top, as opposed to having two pairs of sinks and sources like in the case of the original synaptic placement (Fig. 5F top row; leftmost plot). The firing rate of the L4 excitatory cells, however, remained essentially unchanged by this modification (Fig. 5G). On the other hand, placing all synapses from LGN and excitatory neurons onto the apical dendrites of L4 excitatory neurons resulted in even greater CSD magnitude from this population (Fig. 5F bottom row;

leftmost plot), while the magnitude of its firing rates were reduced (Fig. 5G). In this case, the pattern displayed a sink in the middle with a source above and below it.

These results indicate a two-way dissociation that can occur between CSD and firing rates of excitatory neurons. The firing rates can be changed without substantially changing the CSD by modifying the strength of synapses, while the CSD can be changed without substantially changing the firing rates by modifying synaptic location. This suggests that utilizing the CSD in the optimization of the model can provide constraints on the circuit architecture that could not be obtained from spikes alone.

Effects of feedback from Higher Visual Areas to the model

Hartmann et al. (2019) found that feedback from higher visual areas (HVAs) can exert a powerful influence on the magnitude of the evoked LFP response recorded in V1 of macaque monkeys, particularly in the period 80-100 ms after stimulus onset. The sustained L2/3 sink and L4 source we observe in the experimental CSD emerge at 60 ms (Fig. 2A-B), which roughly coincides with the peak firing rates in the latero-medial (LM), rostro-lateral (RL), antero-lateral (AL), and postero-medial (PM) cortical areas (Fig. 3C). Furthermore, anatomical data indicate that synapses from HVAs terminate on L1 and L2/3 apical dendrites of pyramidal cells (whose cell bodies reside in L2/3 or L5) (Glickfeld and Olsen, 2017; Marques et al., 2018; Hartmann et al., 2019; Keller et al., 2020; Shen et al., 2020). Together, these observations suggest that the sustained L2/3 sink and L4 source might, in part, be induced by feedback from higher visual areas (HVA), where the sink is generated from the input to the apical tufts in L1 and L2/3, and the source may be the return currents of this input.

Of these HVAs, the feedback from LM to V1 is best characterized (Marques et al., 2018; Keller et al., 2020; Shen et al., 2020), and has the highest connection density to V1 (Harris et al., 2019). Based on these considerations, we decided to test the hypothesis that the large sinks and sources in the upper layers were caused, at least in part, by feedback from LM. In addition to the earlier feedforward LGN input and the background input representing the influence of the rest of the brain, we introduced a feedback input constructed from experimentally recorded spike trains in LM. In total, the public Neuropixels dataset has 2075 neurons recorded in LM (simultaneously with the recordings in LGN, V1, and other visual areas) from 42 animals during presentations of the full-field flash stimulus. 1,823 of the 2,075 neurons were classified as RS, and spike trains from these were used to generate the feedback input to the model (Fig. 6A).

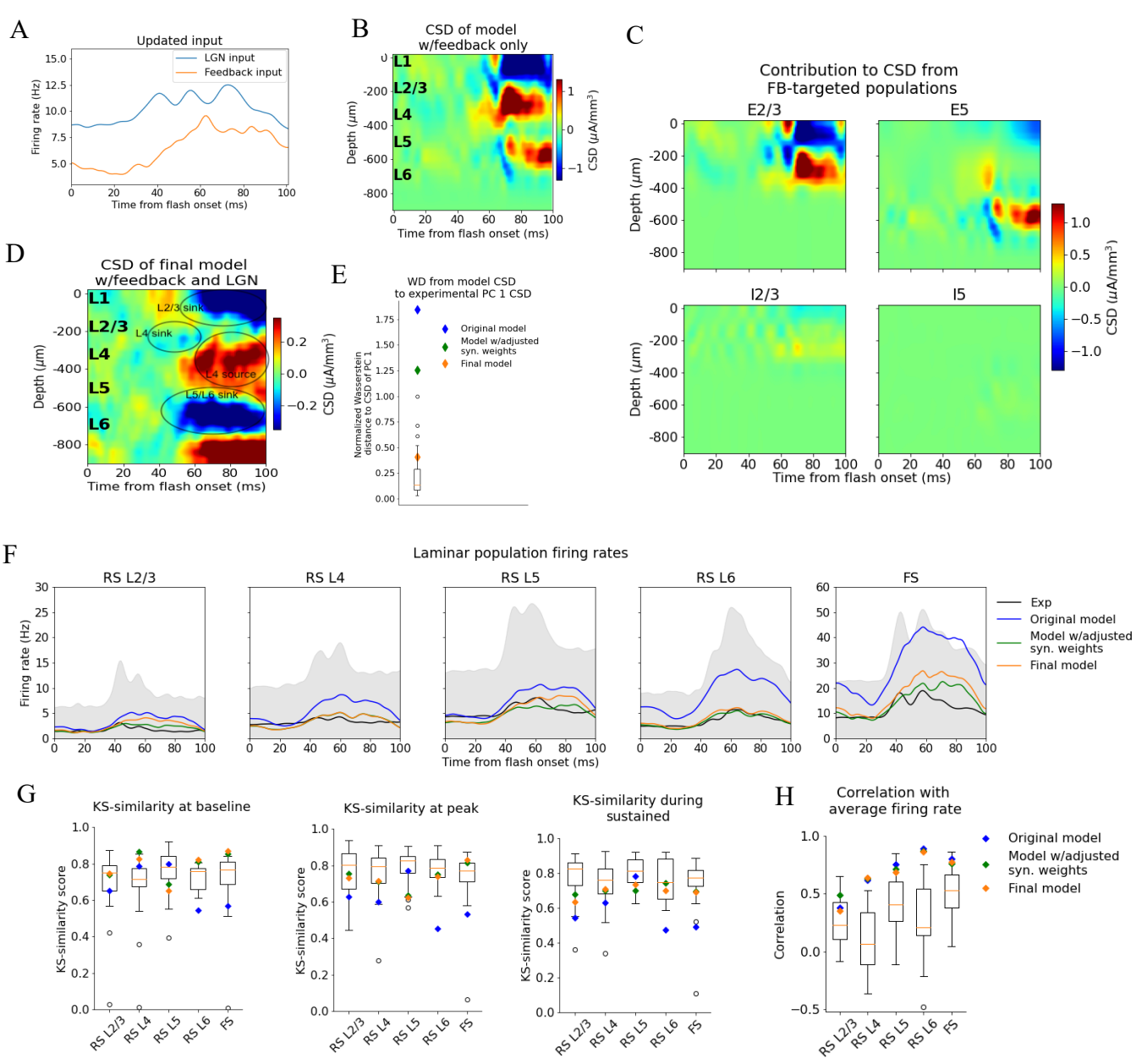

Figure 6: Introducing feedback from LM to V1 in the model. (A) Firing rate of the experimentally recorded LGN and LM units used as input to the model. **(B-C)** Total CSD resulting from simulation with input only from the LM and contributions from populations that receive input from LM. **(D)** Total CSD from simulation with both LGN input and LM input. **(E)** Wasserstein distance between CSD from model versions and PC 1 CSD from experiments together with Wasserstein distances from CSD in animals to PC 1 CSD (boxplot). **(F)** Average population firing rates of experiments (black line) and model versions. **(G)** KS similarity between simulated firing rates or individual animals (boxplots) and recorded firing rates at baseline, peak evoked response, and the sustained period (defined in Fig. 3**).** **(H)** Correlation between simulated and experimentally recorded firing rates (0-100 ms).

The synapses from this LM source were placed on the apical dendrites of L2/3 excitatory neurons (within 150 μm from the soma), on the apical tufts (> 300 μm from the soma) and the basal dendrites (within 150 μm from the soma) of L5 excitatory neurons, and on the somata and basal dendrites of L2/3, and L5 inhibitory (Pvalb and Sst) neurons (at any distance from the soma). The input onto L2/3 excitatory neurons did generate a sink in L1 and L2/3 and a source below in L4 (Fig. 6B-C).

The synaptic weights from LM to the populations targeted by the feedback were initialized at high values (see Methods), and then adjusted (decreased) by multiplying them with factors in the range [0.05, 0.5] (see Methods). The weights from the background to the feedback-targeted populations were also multiplied by factors in the range [0.2, 0.5], and the weights of connections from Pvalb neurons to L2/3 excitatory and L5 excitatory neurons were multiplied by factors in the range [0.8, 1.2]. This weight scaling was done until the population firing rates were within the experimental variability. Additionally, the synapses from excitatory populations onto L6 excitatory cells were restricted to be within 150 μm from the soma to reduce the magnitude of the L5/L6 dipole (Fig. S3) (see Methods).

When the model received this feedback input together with the LGN input, the resulting CSD pattern reproduced the main features observed in the experiments (Fig. 6D). The WD between the model CSD and the experimental PC 1 CSD was also no longer an outlier (Normalized WD = 0.41; Fig. 6E), and the population firing rates remained within the minimum and maximum value of the experimental boxplots for the firing rates in all windows and all populations, both with respect to magnitudes (KSS_b = 0.77, KSS_p = 0.70, and KSS_s = 0.68; average across all populations) and temporal profiles (RS L2/3: r = 0.36***, RS L4: r = 0.64***, RS L5: r = 0.69***, RS L6: r = 0.87***, FS: r = 0.77***, *** p<0.001) (Fig. 6F-G). Thus, when average responses to the full-field flash are considered, this final adjusted model exhibits both the CSD and firing rate patterns that are consistent with the experimental observations and are well within animal variability (Fig. 6E-G).

Identifying the biophysical origins of the canonical CSD

With the canonical CSD (Fig. 2B) reproduced, we can use the model to probe the biophysical origins of its sinks and sources. We began by removing all recurrent connections and only feeding the LGN input to the model to find the contribution from the thalamocortical synapses onto excitatory and inhibitory neurons (Fig. 7A, top). The main thalamic contribution to the CSD is from synapses onto excitatory neurons, in line with the expectation that neurons with a spatial separation between synaptic input currents and the

677 return currents dominate the cortical LFP generation (Einevoll et al., 2013). (Neurons without
678 apical dendrites will have largely overlapping synaptic input currents and return currents,
679 resulting in a cancellation of current sinks and sources.)
680
681 We further observed that the early L4 and the sustained L5/L6 sinks are present in the CSD
682 contributions of excitatory neurons, though the magnitude of the L5/L6 sink is substantially
683 reduced compared to its magnitude when the model is configured with recurrent synapses
684 intact (Fig. 4B, 5D, and 6D). The sustained L2/3 sink and L4 source, on the other hand, were
685 not visible. This suggests that the early L4 sink and the L5/L6 sink are at least partly
686 generated by thalamocortical synapses. However, the substantially diminished magnitude of
687 the L5/L6 sink indicates that recurrent synapses also contribute significantly to the
688 generation of this sink.
689
690 We then removed the LGN input and added the feedback (while keeping the recurrent
691 connections cut), which resulted in a prominent upper layer dipole, with the sink residing in
692 L1 and L2/3, and the source residing in L4 (Fig. 7A, bottom). Together with their absence
693 when input came from LGN only (Fig. 7A, top), this suggests that the sustained L2/3 sink
694 and the L4 source in the canonical pattern originate at least in part from the feedback
695 synapses onto the apical dendrites of L2/3 and L5 pyramidal cells and the activity this input
696 generates.
697
698 To assess the extent to which active channels at the somata contributed to the CSD pattern,
699 we compared the CSD resulting from a simulation with both LGN and feedback input (where
700 the recurrent connections were still cut) when we included or excluded the active channels
701 (NaT, NaP, NaV, h, Kd, Kv2like, Kv3_1, K_T, Im_v2, SK, Ca_HVA, Ca_LVA; only at the
702 soma (see supplementary information in Gouwens et al., 2018 for definitions)) on all neurons
703 in the model. The most prominent discrepancy between the CSD with and without active
704 channels is the magnitude of the L4 source and the L2/3 sink (Fig. 7B). In this all-passive
705 setting, the L4 source is significantly attenuated, and the L2/3 sink is either absent or
706 dominated by a source in the same region.
707
708 We explored whether the contributions from currents in recurrent connections come primarily
709 from excitatory or inhibitory synapses by removing all connections from inhibitory (Pvalb,
710 Sst, Htr3a) neurons to all other neurons, so that all postsynaptic currents stem from
711 excitatory thalamocortical synapses, excitatory synapses from higher visual areas, or
712 recurrent excitatory synapses in V1 (Fig. 7D and Fig. S5). Note that inhibitory synaptic
713 currents give rise to sources, while excitatory synaptic currents give rise to a sink. Of course,

without inhibition, the network is unbalanced, which limits the conclusions that can be drawn from this simulation. However, the fact that the major sinks and sources are still present is an indication that the currents from excitatory input account for the majority of the sinks and sources observed in the experimental CSD.

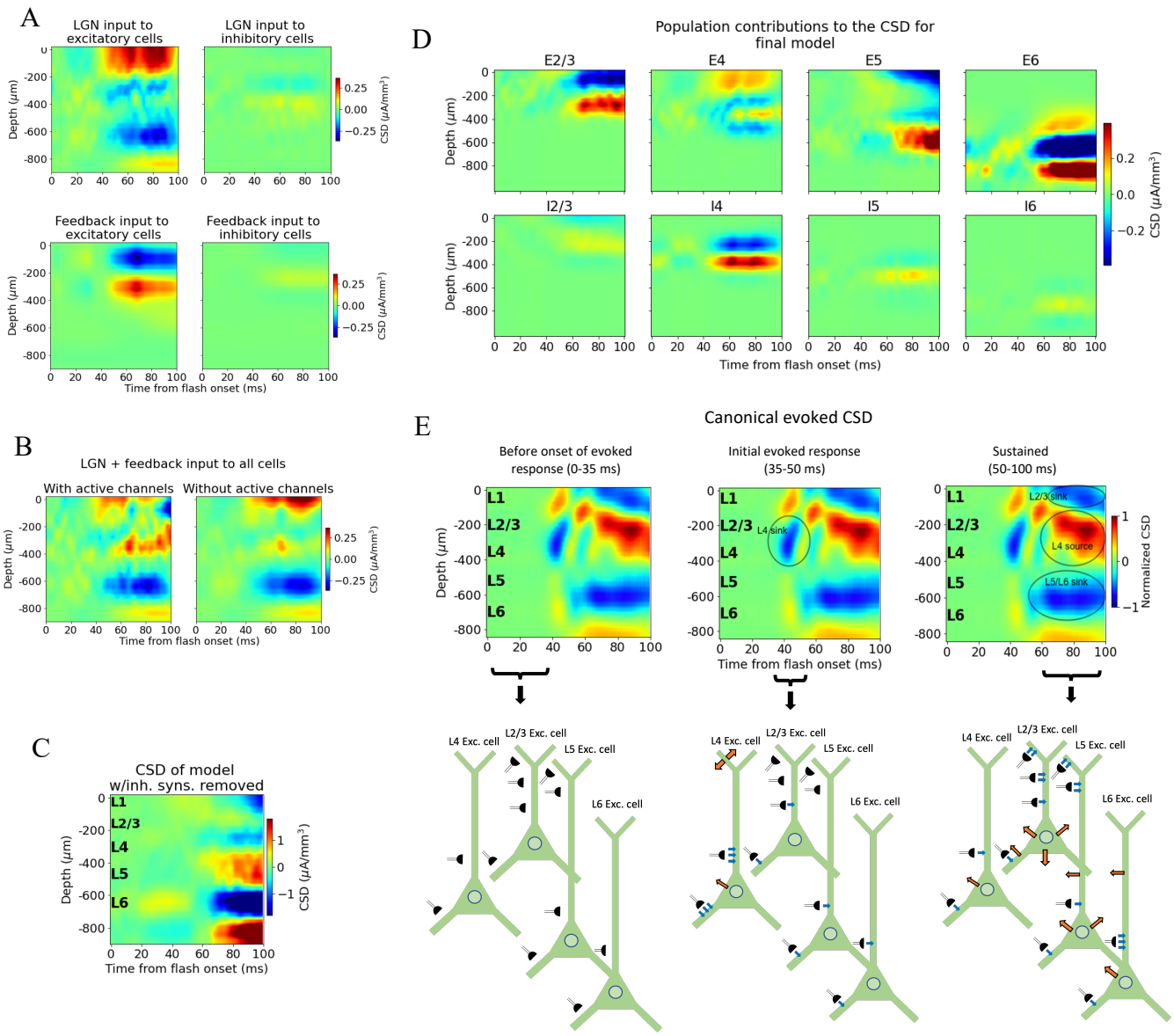

Figure 7: Biophysical origin of canonical CSD. (A) Sinks and sources generated from thalamocortical (top row) and feedback (bottom row) synapses onto excitatory (left) and inhibitory (right) neurons. **(B)** Total CSD from thalamocortical and feedback synapses (without recurrent connections) with (left) and without (right) active channels in the V1 neurons. **(C)** Total CSD of model with both thalamocortical and feedback input when inhibitory synapses are removed. **(D)** Population contributions to the total CSD in final model with both LGN and feedback input and recurrent connections. **(E)** Summary of biophysical origins of the main contributions to the sinks and sources in

749 the canonical CSD in different periods of the first 100 ms after flash onset. Blue arrows indicate
750 inflowing current (sinks), while orange arrows indicate outflowing current (sources) in the illustrations
751 in the bottom. More arrows mean more current. Left: Before onset of evoked response (0-35 ms). The
752 average inflowing and outflowing current in V1 neurons is zero in this time window. Middle: Initial
753 evoked response (35-50 ms). The L4 sink is primarily generated by inflowing current thalamocortical
754 synapses onto L4 excitatory cells. Right: Sustained evoked response (50-100 ms). The L5/L6 sink is
755 primarily due to inflowing currents from thalamocortical synapses and recurrent excitatory synapses.
756 Inflowing current at synapses from HVAs onto apical tufts of L2/3 and L5 excitatory cells generates, in
757 part, the L2/3 sink, and the resulting return current generates, in part, the L4 source in this time
758 window.
759
760 The contributions from each population to the total CSD in the final model (Fig. 6D) with both
761 LGN and feedback input and intact recurrent connections are displayed in Fig. 7D. From
762 this, it is apparent that the L5/L6 dipole is mainly generated by L6 excitatory cells, the L2/3
763 sink stems from sinks at the apical tufts of the L2/3 and L5 excitatory cells, the L4 sink from
764 both the L4 excitatory and inhibitory cells, while the L4 source is a mix of sources from
765 mainly L2/3, L4 and L5 excitatory cells, as well as the L4 inhibitory cells. (The magnitude of
766 the CSD contribution from L4 inhibitory cells is greater than anticipated. Given their lack of
767 apical dendrites, we would expect their postsynaptic current sinks and sources to largely
768 cancel (Einevoll et al., 2013). Their contribution can be reduced by scrambling the 3-D
769 orientation of these cells (Fig. S7). However, we cannot rule out that L4 inhibitory cells can
770 have a contribution comparable in magnitude to the excitatory cells with the data we have
771 available. We therefore let the L4 inhibitory cells keep their original orientation here.)
772
773 We summarize the main contributions to the canonical CSD in Fig. 7E. Before the onset of
774 the evoked response (0-35 ms) there is, on average, no significant net inflow or outflow of
775 current to any neurons. Around 40 ms, an inflow of current from excitatory thalamocortical
776 synapses onto all excitatory neurons and all Pvalb inhibitory neurons appears, with the
777 largest current coming from the synapses targeting basal and apical dendrites of L4
778 excitatory cells. This is the primary origin of the L4 sink. Following this initial L4 sink, there is
779 a sustained sink in L5/L6 arising at ~50 ms, which originates partly from thalamocortical
780 synapses onto L6 excitatory cells and partly from recurrent synapses from excitatory
781 populations in V1 onto L6 excitatory cells. At ~60 ms, a sustained sink emerges in L1 and
782 L2/3, which partly originates in synapses from higher visual areas targeting apical tufts of
783 L2/3 and L5 excitatory cells. This feedback results in a stronger return current at the soma
784 and basal dendrites of L2/3 excitatory cells and L5 excitatory cells.
785

Discussion

In the present study, we analyzed experimentally recorded spikes and LFP during presentation of full-field flashes from a large-scale visual coding dataset derived from mouse visual cortex (Siegle et al., 2021), and simulated the same experimental protocol using a biophysically detailed model of mouse V1 (Billeh et al., 2020). Our analysis of the experimental data focused on the responses in visual areas V1, LGN, and higher cortical visual areas. We found that the evoked CSD in V1, computed from the LFP, is captured by a canonical pattern of sinks and sources during the first 100 ms after stimulus onset (Fig. 2B). This canonical CSD, in response to a flashed, bright field pattern, explains half (50.4 %) of the variance in the trial-averaged CSD responses across animals.

Both the early L4 sink with concurrent sources above and below and the L5/L6 sink with a source below were observed with a similar timing by Senzai, Fernandez-Ruiz, and Buzsáki (2019). The L4 source and L2/3 sink were also observed in that study, but emerge somewhat later than in our data – just after 100 ms as opposed to ~60 ms in our canonical pattern. This discrepancy in onset might simply be due to differences in stimuli. In Senzai, Fernandez-Ruiz, and Buzsáki (2019) the animals were exposed to 100 ms light pulses, while the animals in our data were presented with 250 ms whole-field flashes of white screens. Nonetheless, the canonical CSD pattern exhibits good overall agreement with the pattern seen in Senzai, Fernandez-Ruiz, and Buzsáki (2019).

We introduced the Wasserstein distance as a method to evaluate the difference between two CSD patterns and used it to quantify the variability in trial-averaged CSD between animals (Fig. 2D), the trial-to-trial variability in CSD within animals (Fig. 2F-G), and the difference between the model CSD, the trial-averaged CSD of individual animals, and the canonical CSD pattern. For the firing rate analysis, we utilized KS-similarity and correlation to quantify experimental variability and model performance with regard to magnitude and temporal profile, respectively. Systematic use of quantitative metrics for biophysical modeling at this scale is still relatively uncommon, and our work establishes a set of measures for testing the model on LFP and spiking simultaneously, which can be useful for future studies in the field. Of course, there may well be other metrics that are equally or more suitable, and a systematic investigation into what would be the optimal metrics to apply is a important avenue for future work.

Our aim was to simultaneously reproduce experimentally recorded spikes and CSD in our simulations. The original model captured spiking responses to gratings well (reproducing,

e.g., direction selectivity distributions for different neuronal populations) with variable success when applied to other visual stimuli (Billeh et al., 2020). It was not originally tested on LFP/CSD. We found that, for the full-field flash stimulus, this model did not reproduce the CSD pattern in the upper layers of V1, and the spiking responses for this stimulus also exhibited a number of discrepancies.

After making selective adjustments to the recurrent synaptic weights, the model could reproduce the experimental firing rates (Fig. 5A-C), though the discrepancy between the model CSD and the canonical CSD remained (Fig. 5D-E), with only minor differences relative to the CSD of the original model (Fig. 4B). The fact that the model can capture the experimental firing rates without capturing the experimental CSD and that adjustments to the synaptic weights yielded significant alterations in firing rates with only small changes in the CSD, supports the point that LFP/CSD reflects aspects of circuit dynamics that are complementary to those reflected in locally recorded spikes.

Past simulation studies have demonstrated the importance of synaptic placement in shaping the LFP and CSD signature (Einevoll et al., 2007; Pettersen, Hagen, and Einevoll, 2008; Lindén et al, 2010; Lindén et al, 2011; Łęski et al., 2013; Hagen et al., 2017; Ness et al., 2018). To uncover the model adjustments that capture firing rates and CSD simultaneously, we explored the effects of changes in the synaptic positioning. In one case, we placed all excitatory synapses onto only basal or apical dendrites of L4 excitatory cells, as opposed to their original placement on both apical and basal dendrites. Moving all excitatory synapses onto basal dendrites resulted in substantial changes in both the pattern and magnitude of the CSD contribution from these L4 excitatory cells, with only minor changes to their firing rates (Fig. 5F-G). Placing all excitatory synapses on apical dendrites led to somewhat larger changes in firing rates, though still similar to the firing rate of the original model, and to even bigger changes in the CSD magnitude.

This demonstrates a two-way dissociation of the firing rates and the pattern of sinks and sources in the CSD: The firing rates can be substantially altered with small effects on the CSD by adjusting the synaptic weights, and the CSD can be substantially altered with only small effects on the firing rates by adjusting synaptic placement. This implies that the LFP can reveal deficiencies in the model architecture that would not be evident from the firing rates alone, and that, to a certain extent, models can be optimized for firing rates and CSD independently.

Recent studies have shown that feedback from higher visual areas can exert a strong influence on the magnitude of LFP during evoked responses (Hartmann et al., 2019). To investigate whether such cortico-cortical influence can contribute to the sinks and sources of the canonical CSD pattern, we added feedback consisting of experimentally recorded spikes from the higher cortical visual area LM (Siegle et al., 2021) impinging on synapses placed onto V1 neurons in our model, using anatomical data (Glickfeld and Olsen, 2017; Marques et al., 2018; Hartmann et al., 2019; Keller et al., 2020; Shen et al., 2020). We found that the feedback can play a significant role in shaping the sustained sinks and sources (Fig. 6B-D). The resulting model CSD reproduced the major sinks and sources identified in the canonical CSD pattern and was no longer among the outliers when compared to the experimental variability (Fig. 6E). Interestingly, absence of the feedback was not apparent from analysis of the firing rates alone, as the firing rates were already within the experimental variability before adding the feedback, further underscoring the utility of the LFP in illuminating structure-function relations in the circuit. Contributions from other visual cortical areas were not included, even though they too impinge upon neurons in V1 (Harris et al., 2019; Siegle et al., 2021), due to the lack of data characterizing such connections. This awaits future work.

With the major sinks and sources of the canonical CSD pattern reproduced, we explored their biophysical origins. We found that the initial L4 sink originates in the thalamocortical input to L4 excitatory cells, which aligns with suggestions made in Mitzdorf et al. (1987), Swadlow, Gusev, and Bezdudnaya (2002), and Senzai, Fernandez-Ruiz, and Buzsáki (2019). The sustained L5/L6 sink comes from postsynaptic currents in L6 excitatory cells triggered by a combination of thalamocortical and recurrent excitatory inputs. The sustained L2/3 sink stems, in part, from input from LM onto the apical tufts of L2/3 and L5 excitatory cells. The sustained L4 source has its origins in a mixture of return currents from L2/3 and L5 excitatory cells resulting from the abovementioned feedback onto the apical dendrites of these cells, as well as contributions from L4 excitatory and inhibitory cells (Fig. 7A, D, and E).

In line with observations made by Reimann et al. (2013), we found that the somatic voltage-dependent membrane currents significantly shape the CSD signature (Fig. 5H and 7B). Even so, our findings still emphasize the importance of synaptic inputs in sculpting the CSD, as the addition of synaptic input (Fig. 6D) and changes to synaptic placement (Fig. 5F) substantially altered the CSD pattern.

This investigation into the biophysical origins of sinks and sources is limited by the fact that the contributions from recurrent connections are difficult to estimate precisely due to the non-

linear effects of these connections in terms of how they contribute to spiking. That is, their contribution cannot simply be found by subtracting the CSD from thalamocortical and feedback synapses with all recurrent connections removed (Fig. 7A) from the total CSD with the same input and recurrent connections intact (Fig. 6D). Still, this analysis provides an initial estimate into the biophysical origins of the sinks and sources observed experimentally and demonstrates the insights that can be obtained from modeling of extracellular signals.

There is ample evidence that firing rates and LFP are modulated by the behavioral state of the animal, including measures like the pupil size (considered to be a proxy for arousal level) or running speed (Niell and Stryker, 2010; McGinley et al., 2015; Vinck et al., 2015; Saleem et al., 2017). In this study, the responses averaged over all trials have been the target for the modeling, without regard to any state-dependence of the responses. Our understanding of the state-dependent responses could benefit from the potential to probe the biophysical origins of extracellular signals. Therefore, reproducing these state-dependent responses is an interesting avenue for future research.

Note that the set of synaptic weights and other parameters that can reproduce the experimental firing rates and CSD is unlikely to be unique. This is a consequence of the degeneracy inherent to neural networks, as many different parameterizations of neuronal networks can perform the same functions (Prinz, Bucher and Marder, 2004; Marder and Goaillard, 2006; Drion, O'Leary and Marder, 2015; O'Leary, 2018). Thus, our network should only be considered an example of a circuit model that can produce firing rates and CSD that match the experimental observations. Obtaining multiple solutions and characterizing their diversity using automatic searches of the parameter space will be an interesting direction for future work. We did not utilize such an approach here because the number of simulations required (typically, many thousands or more for automatic optimization approaches) would currently be prohibitively expensive on a model of this scale and level of complexity: running a 1 second simulation with this model takes ~90 minutes on 384 CPU-cores (Billeh et al., 2020); a single trial in our simulations lasts 0.75 seconds.

The original model used as a starting point here produced firing rates and direction and orientation tuning consistent with recordings during presentations of drifting gratings (Arkhipov et al., 2018; Billeh et al., 2020). In this study, we focused on the analysis and modeling of the response to full-field flashes. Ideally, the model should reproduce both firing rates and LFP simultaneously not only for flashes or drifting gratings, but for any visual stimulus (out-class generalization). This is a long-term goal, and can be called "the holy grail" of visual system modeling.

In this study, we developed a systematic framework to quantify experimental variability in both LFP/CSD and spikes and to evaluate model performance. We identified a canonical CSD pattern observed during presentations of full-field flash stimuli and obtained a bio-realistic model that reproduced both the canonical CSD pattern and spikes simultaneously. We utilized this validated model to identify the biophysical origins of the canonical sinks and sources observed experimentally. Our models are freely shared and should be useful for future studies disentangling the mechanisms underlying spiking dynamics and electrogenesis in the cortex.

Acknowledgements

Research reported in this publication was supported the Simula School of Research and Innovation, CINPLA, the European Union Horizon 2020 Research and Innovation Program under Grant Agreement No. 785907 and No. 945539 (Human Brain Project (HBP) SGA2 and SGA3), the National Institute of Neurological Disorders and Stroke of the National Institutes of Health under Award Number R01NS122742, and by the National Institute Of Biomedical Imaging And Bioengineering of the National Institutes of Health under Award Number R01EB029813. The content is solely the responsibility of the authors and does not necessarily represent the official views of the National Institutes of Health. We acknowledge the use of Fenix Infrastructure resources, which are partially funded from the European Union's Horizon 2020 research and innovation program through the ICEI project under the grant agreement No. 800858. We thank the Allen Institute founder, Paul G. Allen, for his vision, encouragement, and support.

References

Andersen, R.A., Musallam, S., Pesaran, B., 2004. Selecting the signals for a brain–machine interface. Curr. Opin. Neurobiol. 14, 720–726. https://doi.org/10.1016/J.CONB.2004.10.005

Arjovsky, M., Chintala, S., Bottou, L., 2017. Wasserstein generative adversarial networks, in: International Conference on Machine Learning. pp. 214–223.

Arkhipov, A., Gouwens, N.W., Billeh, Y.N., Gratiy, S., Iyer, R., Wei, Z., Xu, Z., Abbasi-Asl, R., Berg, J., Buice, M., Cain, N., Costa, N. da, Vries, S. de, Denman, D., Durand, S., Feng, D., Jarsky, T., Lecoq, J., Lee, B., Li, L., Mihalas, S., Ocker, G.K., Olsen, S.R., Reid, R.C., Soler-Llavina, G., Sorensen, S.A., Wang, Q., Waters, J., Scanziani, M., Koch, C., 2018. Visual physiology of the layer 4 cortical circuit in silico. PLOS Comput. Biol. 14, e1006535. https://doi.org/10.1371/JOURNAL.PCBI.1006535

Bastos, A.M., Vezoli, J., Bosman, C.A., Schoffelen, J.M., Oostenveld, R., Dowdall, J.R., DeWeerd, P., Kennedy, H., Fries, P., 2015. Visual Areas Exert Feedforward and Feedback Influences through Distinct Frequency Channels. Neuron 85, 390–401. https://doi.org/10.1016/J.NEURON.2014.12.018

Barthó, P., Hirase, H., Monconduit, L., Zugaro, M., Harris, K.D. and Buzsaki, G., 2004. Characterization of neocortical principal cells and interneurons by network interactions and extracellular features. *Journal of neurophysiology*, *92*(1), pp.600-608. https://doi.org/10.1152/jn.01170.2003

Belitski, A., Gretton, A., Magri, C., Murayama, Y., Montemurro, M.A., Logothetis, N.K., Panzeri, S., 2008. Low-Frequency Local Field Potentials and Spikes in Primary Visual Cortex Convey Independent Visual Information. J. Neurosci. 28, 5696–5709. https://doi.org/10.1523/JNEUROSCI.0009-08.2008

Billeh, Y.N., Cai, B., Gratiy, S.L., Dai, K., Iyer, R., Gouwens, N.W., Abbasi-Asl, R., Jia, X., Siegle, J.H., Olsen, S.R., Koch, C., Mihalas, S., Arkhipov, A., 2020. Systematic Integration of Structural and Functional Data into Multi-scale Models of Mouse Primary Visual Cortex. Neuron 106, 388-403.e18. https://doi.org/10.1016/j.neuron.2020.01.040

Buzsáki, G., 2006. *Rhythms of the Brain*. Oxford university press.

Buzsáki, G., Anastassiou, C.A. and Koch, C., 2012. The origin of extracellular fields and currents—EEG, ECoG, LFP and spikes. *Nature reviews neuroscience*, *13*(6), pp.407-420. doi: 10.1038/nrn3241

999 Chatzikalymniou, A.P. and Skinner, F.K., 2018. Deciphering the contribution of oriens-
1000 lacunosum/moleculare (OLM) cells to intrinsic θ rhythms using biophysical local field
1001 potential (LFP) models. *Eneuro*, *5*(4). 10.1523/ENEURO.0146-18.2018
1002
1003 Dai, K., Gratiy, S.L., Billeh, Y.N., Xu, R., Cai, B., Cain, N., Rimehaug, A.E., Stasik, A.J.,
1004 Einevoll, G.T., Mihalas, S., Koch, C., Arkhipov, A., 2020. Brain Modeling ToolKit: An
1005 open source software suite for multiscale modeling of brain circuits. PLoS Comput.
1006 Biol. 16. https://doi.org/10.1371/journal.pcbi.1008386
1007
1008 Di, S., Baumgartner, C., Barth, D.S., 1990. Laminar analysis of extracellular field potentials
1009 in rat vibrissa/barrel cortex. J. Neurophysiol. 63, 832–840.
1010 https://doi.org/10.1152/JN.1990.63.4.832
1011
1012 Drion, G., O'Leary, T., Marder, E., 2015. Ion channel degeneracy enables robust and
1013 tunable neuronal Firing rates. Proc. Natl. Acad. Sci. U. S. A. 112, E5361–E5370.
1014 https://doi.org/10.1073/pnas.1516400112
1015
1016 Einevoll, G.T., Pettersen, K.H., Devor, A., Ulbert, I., Halgren, E., Dale, A.M., 2007. Laminar
1017 population analysis: Estimating firing rates and evoked synaptic activity from
1018 multielectrode recordings in rat barrel cortex. J. Neurophysiol. 97, 2174–2190.
1019 https://doi.org/10.1152/jn.00845.2006
1020
1021 Einevoll, G.T., Kayser, C., Logothetis, N.K. and Panzeri, S., 2013. Modelling and analysis of
1022 local field potentials for studying the function of cortical circuits. Nature Reviews
1023 Neuroscience, 14(11), pp.770-785. https://doi.org/10.1038/nrn3599
1024
1025 Głąbska, H., Chintaluri, H.C. and Wójcik, D.K., 2014. Collection of simulated data for
1026 validation of methods of analysis of extracellular potentials. *Neuroinformatics*
1027 10.3389/conf.fninf.2014.18.00035
1028
1029 Glickfeld, L.L., Olsen, S.R., 2017. The Annual Review of Vision Science is online at. Annu
1030 Rev Vis Sci 3, 251–73. https://doi.org/10.1146/annurev-vision-102016
1031
1032 Gouwens, N.W., Berg, J., Feng, D., Sorensen, S.A., Zeng, H., Hawrylycz, M.J., Koch, C.,
1033 Arkhipov, A., 2018. Systematic generation of biophysically detailed models for

diverse cortical neuron types. Nat. Commun. 9. https://doi.org/10.1038/s41467-017-02718-3

Hagen, E., Dahmen, D., Stavrinou, M.L., Lindén, H., Tetzlaff, T., Albada, S.J.V., Grün, S., Diesmann, M., Einevoll, G.T., 2016. Hybrid scheme for modeling local field potentials from point-neuron networks. Cereb. Cortex 26, 4461–4496. https://doi.org/10.1093/cercor/bhw237

Hagen, E., Fossum, J.C., Pettersen, K.H., Alonso, J.M., Swadlow, H.A. and Einevoll, G.T., 2017. Focal local field potential signature of the single-axon monosynaptic thalamocortical connection. Journal of Neuroscience, 37(20), pp.5123-5143. https://doi.org/10.1523/JNEUROSCI.2715-16.2017

Hagen, E., Næss, S., Ness, T.V. and Einevoll, G.T., 2018. Multimodal modeling of neural network activity: computing LFP, ECoG, EEG, and MEG signals with LFPy 2.0. *Frontiers in neuroinformatics*, *12*, p.92. https://doi.org/10.3389/fninf.2018.00092

Harris, J.A., Mihalas, S., Hirokawa, K.E., Whitesell, J.D., Choi, H., Bernard, A., Bohn, P., Caldejon, S., Casal, L., Cho, A., Feiner, A., Feng, D., Gaudreault, N., Gerfen, C.R., Graddis, N., Groblewski, P.A., Henry, A.M., Ho, A., Howard, R., Knox, J.E., Kuan, L., Kuang, X., Lecoq, J., Lesnar, P., Li, Y., Luviano, J., McConoughey, S., Mortrud, M.T., Naeemi, M., Ng, L., Oh, S.W., Ouellette, B., Shen, E., Sorensen, S.A., Wakeman, W., Wang, Q., Wang, Y., Williford, A., Phillips, J.W., Jones, A.R., Koch, C., Zeng, H., 2019. Hierarchical organization of cortical and thalamic connectivity. Nature 575, 195–202. https://doi.org/10.1038/s41586-019-1716-z

Hartmann, T.S., Raja, S., Lomber, S.G., Born, R.T., 2019. Cortico-cortical feedback from V2 exerts a powerful influence over the visually evoked local field potential and associated spike timing in V1. bioRxiv. https://doi.org/10.1101/792010

Hay, E., Hill, S., Schürmann, F., Markram, H. and Segev, I., 2011. Models of neocortical layer 5b pyramidal cells capturing a wide range of dendritic and perisomatic active properties. *PLoS computational biology*, *7*(7), p.e1002107. https://doi.org/10.1371/journal.pcbi.1002107

Henrie, J.A., Shapley, R., 2005. LFP Power Spectra in V1 Cortex: The Graded Effect of Stimulus Contrast. J Neurophysiol 94, 479–490. https://doi.org/10.1152/jn.00919.2004

Holt, G.R., Koch, C., 1999. Electrical Interactions via the Extracellular Potential Near Cell Bodies, Journal of Computational Neuroscience.

Jun, J.J., Steinmetz, N.A., Siegle, J.H., Denman, D.J., Bauza, M., Barbarits, B., Lee, A.K., Anastassiou, C.A., Andrei, A., Aydın, Ç. and Barbic, M., 2017. Fully integrated silicon probes for high-density recording of neural activity. Nature, 551(7679), p https://doi.org/10.1038/nature24636

Kandel, A., Buzsá, G.R., 1997. Cellular-Synaptic Generation of Sleep Spindles, Spike-and-Wave Discharges, and Evoked Thalamocortical Responses in the Neocortex of the Rat. J. Neurosci. 17, 6783–6797. https://doi.org/10.1523/JNEUROSCI.17-17-06783.1997

Keller, A.J., Roth, M.M., Scanziani, M., 2020. Feedback generates a second receptive field in neurons of the visual cortex. Nature 582, 545–549. https://doi.org/10.1038/s41586-020-2319-4

Koch, C., 1999. Biophysics of computation: information processing in single neurons. Oxford university press.

Kreiman, G., Hung, C.P., Kraskov, A., Quiroga, R.Q., Poggio, T., DiCarlo, J.J., 2006. Object Selectivity of Local Field Potentials and Spikes in the Macaque Inferior Temporal Cortex. Neuron 49, 433–445. https://doi.org/10.1016/J.NEURON.2005.12.019

Łęski, S., Lindén, H., Tetzlaff, T., Pettersen, K.H., Einevoll, G.T., 2013. Frequency Dependence of Signal Power and Spatial Reach of the Local Field Potential. PLoS Comput. Biol. 9. https://doi.org/10.1371/journal.pcbi.1003137

Liebe, S., Hoerzer, G.M., Logothetis, N.K., Rainer, G., 2012. Theta coupling between V4 and prefrontal cortex predicts visual short-term memory performance. Nat. Neurosci. 2012 153 15, 456–462. https://doi.org/10.1038/nn.3038

Lindén, H., Pettersen, K.H., Einevoll, G.T., 2010. Intrinsic dendritic filtering gives low-pass power spectra of local field potentials. J. Comput. Neurosci. 29, 423–444. https://doi.org/10.1007/s10827-010-0245-4

Lindén, H., Tetzlaff, T., Potjans, T.C., Pettersen, K.H., Grün, S., Diesmann, M., Einevoll, G.T., 2011. Modeling the spatial reach of the LFP. Neuron 72, 859–872. https://doi.org/10.1016/j.neuron.2011.11.006

Liu, J., Newsome, W.T., 2006. Local Field Potential in Cortical Area MT: Stimulus Tuning and Behavioral Correlations. J. Neurosci. 26, 7779–7790. https://doi.org/10.1523/JNEUROSCI.5052-05.2006

Marder, E. and Goaillard, J.M., 2006. Variability, compensation and homeostasis in neuron and network function. Nature Reviews Neuroscience, 7(7), pp.563-574. https://doi.org/10.1038/nrn1949

Markowitz, D.A., Wong, Y.T., Gray, C.M., Pesaran, B., 2011. Optimizing the Decoding of Movement Goals from Local Field Potentials in Macaque Cortex. J. Neurosci. 31, 18412–18422. https://doi.org/10.1523/JNEUROSCI.4165-11.2011

Marques, T., Nguyen, J., Fioreze, G., Petreanu, L., 2018. The functional organization of cortical feedback inputs to primary visual cortex. Nat. Neurosci. 21, 757–764. https://doi.org/10.1038/s41593-018-0135-z

McGinley, M.J., Vinck, M., Reimer, J., Batista-Brito, R., Zagha, E., Cadwell, C.R., Tolias, A.S., Cardin, J.A., McCormick, D.A., 2015. Waking State: Rapid Variations Modulate Neural and Behavioral Responses. Neuron 87, 1143–1161. https://doi.org/10.1016/J.NEURON.2015.09.012

Mehring, C., Rickert, J., Vaadia, E., Oliveira, S.C.D., Aertsen, A., Rotter, S., 2003. Inference of hand movements from local field potentials in monkey motor cortex. Nat. Neurosci. 2003 612 6, 1253–1254. https://doi.org/10.1038/nn1158

Mitzdorf, U., 1985. Current source-density method and application in cat cerebral cortex: investigation of evoked potentials and EEG phenomena. *Physiological reviews*, *65*(1), pp.37-100. https://doi.org/10.1152/physrev.1985.65.1.37

Mitzdorf, U., 1987. Properties of the evoked potential generators: current source-density analysis of visually evoked potentials in the cat cortex. *International Journal of Neuroscience*, *33*(1-2), pp.33-59. https://doi.org/10.3109/00207458708985928

Montemurro, M.A., Rasch, M.J., Murayama, Y., Logothetis, N.K., Panzeri, S., 2008. Phase-of-Firing Coding of Natural Visual Stimuli in Primary Visual Cortex. Curr. Biol. 18, 375–380. https://doi.org/10.1016/J.CUB.2008.02.023

Mukamel, R., Fried, I., 2012. Human intracranial recordings and cognitive neuroscience. Annu. Rev. Psychol. 63, 511–537. https://doi.org/10.1146/annurev-psych-120709-145401

Nauhaus, I., Busse, L., Carandini, M., Ringach, D.L., 2008. Stimulus contrast modulates functional connectivity in visual cortex. Nat. Neurosci. 2008 121 12, 70–76. https://doi.org/10.1038/nn.2232

Ness, T.V., Remme, M.W. and Einevoll, G.T., 2018. h-Type membrane current shapes the local field potential from populations of pyramidal neurons. *Journal of Neuroscience*, *38*(26), pp.6011-6024. DOI: https://doi.org/10.1523/JNEUROSCI.3278-17.2018

Niell, C.M., Stryker, M.P., 2008. Highly Selective Receptive Fields in Mouse Visual Cortex. J. Neurosci. 28, 7520–7536. https://doi.org/10.1523/JNEUROSCI.0623-08.2008

Niell, C.M., Stryker, M.P., 2010. Modulation of Visual Responses by Behavioral State in Mouse Visual Cortex. Neuron 65, 472–479. https://doi.org/10.1016/j.neuron.2010.01.033

Oh, S.W., Harris, J.A., Ng, L., Winslow, B., Cain, N., Mihalas, S., Wang, Q., Lau, C., Kuan, L., Henry, A.M., Mortrud, M.T., Ouellette, B., Nguyen, T.N., Sorensen, S.A., Slaughterbeck, C.R., Wakeman, W., Li, Y., Feng, D., Ho, A., Nicholas, E., Hirokawa, K.E., Bohn, P., Joines, K.M., Peng, H., Hawrylycz, M.J., Phillips, J.W., Hohmann, J.G., Wohnoutka, P., Gerfen, C.R., Koch, C., Bernard, A., Dang, C., Jones, A.R.,

Zeng, H., 2014. A mesoscale connectome of the mouse brain. Nat. 2014 5087495 508, 207–214. https://doi.org/10.1038/nature13186

O'Leary, T., 2018. Homeostasis, failure of homeostasis and degenerate ion channel regulation. *Current Opinion in Physiology*, *2*, pp.129-138. https://doi.org/10.1016/j.cophys.2018.01.006

Pesaran, B., Pezaris, J.S., Sahani, M., Mitra, P.P., Andersen, R.A., 2002. Temporal structure in neuronal activity during working memory in macaque parietal cortex. Nat. Neurosci. 2002 58 5, 805–811. https://doi.org/10.1038/nn890

Pesaran, B., Vinck, M., Einevoll, G.T., Sirota, A., Fries, P., Siegel, M., Truccolo, W., Schroeder, C.E. and Srinivasan, R., 2018. Investigating large-scale brain dynamics using field potential recordings: analysis and interpretation. *Nature neuroscience*, *21*(7), pp.903-919. https://doi.org/10.1038/s41593-018-0171-8

Pettersen, K.H., Devor, A., Ulbert, I., Dale, A.M., Einevoll, G.T., 2006. Current-source density estimation based on inversion of electrostatic forward solution: Effects of finite extent of neuronal activity and conductivity discontinuities. J. Neurosci. Methods 154, 116–133. https://doi.org/10.1016/j.jneumeth.2005.12.005

Pettersen, K.H., Hagen, E. and Einevoll, G.T., 2008. Estimation of population firing rates and current source densities from laminar electrode recordings. *Journal of computational neuroscience*, *24*(3), pp.291-313. https://doi.org/10.1007/s10827-007-0056-4

Pettersen, K.H. and Einevoll, G.T., 2008. Amplitude variability and extracellular low-pass filtering of neuronal spikes. *Biophysical journal*, *94*(3), pp.784-802. https://doi.org/10.1529/biophysj.107.111179

Prinz, A.A., Bucher, D., Marder, E., 2004. Similar network activity from disparate circuit parameters. Nat. Neurosci. 7, 1345–1352. https://doi.org/10.1038/nn1352

Rall, W., 1962. Electrophysiology of a Dendritic Neuron Model. Biophys. J. 2, 145. https://doi.org/10.1016/S0006-3495(62)86953-7

Reimann, M.W., Anastassiou, C.A., Perin, R., Hill, S.L., Markram, H., Koch, C., 2013. A biophysically detailed model of neocortical local field potentials predicts the critical role of active membrane currents. Neuron 79, 375–390. https://doi.org/10.1016/j.neuron.2013.05.023

Rickert, J., Oliveira, S.C.D., Vaadia, E., Aertsen, A., Rotter, S., Mehring, G., 2005. Encoding of Movement Direction in Different Frequency Ranges of Motor Cortical Local Field Potentials. J. Neurosci. 25, 8815–8824. https://doi.org/10.1523/JNEUROSCI.0816-05.2005

Roux, S., MacKay, W.A., Riehle, A., 2006. The pre-movement component of motor cortical local field potentials reflects the level of expectancy. Behav. Brain Res. 169, 335–351. https://doi.org/10.1016/j.bbr.2006.02.004

Rubner, Y., Tomasi, C., Guibas, L.J., 1998. A metric for distributions with applications to image databases, in: Sixth International Conference on Computer Vision (IEEE Cat. No. 98CH36271). pp. 59–66. 10.1109/ICCV.1998.710701

Saleem, A.B., Lien, A.D., Krumin, M., Haider, B., Rosón, M.R., Ayaz, A., Reinhold, K., Busse, L., Carandini, M., Harris, K.D., Carandini, M., 2017. Subcortical Source and Modulation of the Narrowband Gamma Oscillation in Mouse Visual Cortex. Neuron 93, 31https://doi.org/10.1016/j.neuron.2016.12.028

Scherberger, H., Jarvis, M.R., Andersen, R.A., 2005. Cortical Local Field Potential Encodes Movement Intentions in the Posterior Parietal Cortex. Neuron 46, 347–354. https://doi.org/10.1016/J.NEURON.2005.03.004

Schomburg, E.W., Anastassiou, C.A., Buzsáki, G. and Koch, C., 2012. The spiking component of oscillatory extracellular potentials in the rat hippocampus. *Journal of Neuroscience*, *32*(34), pp.11798-11811. https://doi.org/10.1523/JNEUROSCI.0656-12.2012

Shen, S., Jiang, X., Scala, F., Fu, J., Fahey, P., Kobak, D., Tan, Z., Reimer, J., Sinz, F., Tolias, A.S., 2020. Distinct organization of two cortico-cortical feedback pathways. bioRxiv. https://doi.org/10.1101/2020.02.27.968792

Senzai, Y., Fernandez-Ruiz, A. and Buzsáki, G., 2019. Layer-specific physiological features and interlaminar interactions in the primary visual cortex of the mouse. Neuron, 101(3), pp.500-513. 10.1016/j.neuron.2018.12.009

Siegle, J.H., Jia, X., Durand, S., Gale, S., Bennett, C., Graddis, N., Heller, G., Ramirez, T.K., Choi, H., Luviano, J.A., Groblewski, P.A., Ahmed, R., Arkhipov, A., Bernard, A., Billeh, Y.N., Brown, D., Buice, M.A., Cain, N., Caldejon, S., Casal, L., Cho, A., Chvilicek, M., Cox, T.C., Dai, K., Denman, D.J., Vries, S.E.J. de, Dietzman, R., Esposito, L., Farrell, C., Feng, D., Galbraith, J., Garrett, M., Gelfand, E.C., Hancock, N., Harris, J.A., Howard, R., Hu, B., Hytnen, R., Iyer, R., Jessett, E., Johnson, K., Kato, I., Kiggins, J., Lambert, S., Lecoq, J., Ledochowitsch, P., Lee, J.H., Leon, A., Li, Y., Liang, E., Long, F., Mace, K., Melchior, J., Millman, D., Mollenkopf, T., Nayan, C., Ng, L., Ngo, K., Nguyen, T., Nicovich, P.R., North, K., Ocker, G.K., Ollerenshaw, D., Oliver, M., Pachitariu, M., Perkins, J., Reding, M., Reid, D., Robertson, M., Ronellenfitch, K., Seid, S., Slaughterbeck, C., Stoecklin, M., Sullivan, D., Sutton, B., Swapp, J., Thompson, C., Turner, K., Wakeman, W., Whitesell, J.D., Williams, D., Williford, A., Young, R., Zeng, H., Naylor, S., Phillips, J.W., Reid, R.C., Mihalas, S., Olsen, S.R., Koch, C., 2021. Survey of spiking in the mouse visual system reveals functional hierarchy. Nature 592, 86–92. https://doi.org/10.1038/s41586-020-03171-x

Sinha, M. and Narayanan, R., 2015. HCN channels enhance spike phase coherence and regulate the phase of spikes and LFPs in the theta-frequency range. *Proceedings of the National Academy of Sciences*, *112*(17), pp.E2207-E2216. https://doi.org/10.1073/pnas.1419017112

Sinha, M. and Narayanan, R., 2021. Active Dendrites and Local Field Potentials: Biophysical Mechanisms and Computational Explorations. *neuroscience*. https://doi.org/10.1016/j.neuroscience.2021.08.035

Stavisky, S.D., Kao, J.C., Nuyujukian, P., Ryu, S.I., Shenoy, K.V., 2015. A high performing brain-machine interface driven by low-frequency local field potentials alone and together with spikes. J. Neural Eng. 12. https://doi.org/10.1088/1741-2560/12/3/036009

Swadlow, H.A., Gusev, A.G. and Bezdudnaya, T., 2002. Activation of a cortical column by a thalamocortical impulse. *Journal of Neuroscience*, *22*(17), pp.7766-7773. https://doi.org/10.1523/JNEUROSCI.22-17-07766.2002

Traub, R.D., Contreras, D., Cunningham, M.O., Murray, H., LeBeau, F.E.N., Roopun, A., Bibbig, A., Wilent, W.B., Higley, M.J., Whittington, M.A., 2005. Single-column thalamocortical network model exhibiting gamma oscillations, sleep spindles, and epileptogenic bursts. J. Neurophysiol. 93, 2194–2232. https://doi.org/10.1152/jn.00983.2004

Tomsett, R.J., Ainsworth, M., Thiele, A., Sanayei, M., Chen, X., Gieselmann, M.A., Whittington, M.A., Cunningham, M.O. and Kaiser, M., 2015. Virtual Electrode Recording Tool for EXtracellular potentials (VERTEX): comparing multi-electrode recordings from

Victor, J.D., Purpura, K., Katz, E., Mao, B., 1994. Population encoding of spatial frequency, orientation, and color in macaque V1. J. Neurophysiol. 72, 2151–2166. https://doi.org/10.1152/JN.1994.72.5.2151

Vinck, M., Batista-Brito, R., Knoblich, U., Cardin, J.A., 2015. Arousal and Locomotion Make Distinct Contributions to Cortical Activity Patterns and Visual Encoding. Neuron 86, 740–754. https://doi.org/10.1016/j.neuron.2015.03.028

Vierling-Claassen, D., Cardin, J., Moore, C.I. and Jones, S.R., 2010. Computational modeling of distinct neocortical oscillations driven by cell-type selective optogenetic drive: separable resonant circuits controlled by low-threshold spiking and fast-spiking interneurons. *Frontiers in human neuroscience*, *4*, p.198. https://doi.org/10.3389/fnhum.2010.00198

Womelsdorf, T., Fries, P., Mitra, P.P., Desimone, R., 2005. Gamma-band synchronization in visual cortex predicts speed of change detection. Nat. 2006 4397077 439, 733–736. https://doi.org/10.1038/nature04258

Methods

Experiments

Quality control

Of the 58 mice in the visual coding dataset, nine were excluded because the exact probe location could not be recovered due to fading of fluorescent dye or artifacts in the optical projection tomography (OPT) volume (Siegle et al., 2021). Another five animals were excluded because they were missing LFP recordings from V1 during presentation of the flash stimulus. Thus, data for 44 animals were retained for the CSD analysis.

For the spike analysis, the same nine animals for which the exact probe location could not be recovered were excluded, and two additional animals were excluded because they did not have any cells recorded in V1, leaving a total of 47 animals for this part of the data analysis.

Neuronal classification

We distinguished between regular-spiking (RS) and fast-spiking (FS) cells by the time from trough to peak of the spike waveforms (Barthó et al., 2004). For cortical cells, the spike duration was bimodally distributed with a dip at ~0.4 ms, while for thalamic cells, it was bimodally distributed with a dip at ~0.3 ms (Fig. S1). Thus, the cut off in the classification of cells as RS or FS was set at 0.4 ms for LM and V1, and at 0.3 ms for cells in LGN.

When comparing the model firing rates to the experimental firing rates, the excitatory and non-Pvalb populations were grouped together in each layer of the model to make up the RS cells in L2/3, L4, L5, and L6, while the Pvalb cells across all layers were grouped together to make up the FS cells of V1. The layer boundaries were taken from the Allen Common Coordinate Framework (CCF) (Oh et al., 2014), allowing for the assignment of each neuron's position to a specific cortical layer (Siegle et al., 2021).

Model

The model contains a total of 230,924 neurons, of which 51,978 are biophysically detailed multicompartment neurons with somatic Hodkin-Huxley conductances and passive dendrites, and 178,946 are leaky-integrate-and-fire (LIF) neurons. The neuron models are arranged in a cylinder with a radius 845 μm and a height 860 μm (corresponding to the average cortical thickness of V1 taken from the Allen Common Cordinate Framework (CCF) (Billeh et al., 2020; Oh et al., 2014). The multicompartment neurons are placed in the "core"

of the model with a radius of 400 μm, while the LIF neurons form an annulus surrounding this core. The neuron models belong to 17 different classes: one excitatory class and three inhibitory (Pvalb, Sst, Htr3a) in each of the layers 2/3 through 6, and a single Htr3a inhibitory class in layer 1. The LGN module providing thalamocortical input to the model consists of 17,400 units selectively connected to the excitatory neurons and Pvalb neurons in L2/3 to L6, as well as the non-Pvalb neurons in L1. The background input to all neurons in the model comes from a single Poisson source firing at 1 kHz and represents influence from the rest of the brain. The feedback input to L2/3 and L5 excitatory, Pvalb, and Sst neurons comes from a node representing LM.

Simulation configuration

Instructions on how to run simulations of the model are provided in Billeh et al., 2020. The files and code necessary to run the model versions presented in Fig. 4, 5, and 6 are provided in the directories old_model_fig4, intermediate_model_fig5, and final_model_fig6, respectively, in the Dropbox folder (see Code and data availability).

Data processing

LFP and CSD

The LFP in simulations was obtained from the extracellular potential by first downsampling to every other electrode along the probe (resulting in a spatial separation of 40 μm between each recording electrode, equal to the spacing in the public Neuropixels data) and using a low-pass 5^{th} order Butterworth filter with a cut off frequency of 500 Hz (utilizing functions scipy.signal.butter and scipy.signal.filtfilt). The same filtering was applied to get the experimental LFP. The CSD was calculated from the experimental and model LFP using the delta iCSD method (Pettersen et al., 2006), where the radius of laterally (orthogonal to the probe axis) constant CSD was assumed to be 400 μm - the radius of the V1 model's "core" region consisting of biophysically detailed multicompartment neurons. For the experimental CSD, this radius was set to 800 μm, roughly corresponding to the size of mouse V1.

Visual stimulus

The stimulus used to compare the model and the experiments was full-field flashes. In the experiments, the mice were presented with gray screens for 1 second, followed by 250 ms of white screen, and then 750 ms of gray screen over 75 trials. In the simulations, both the stimulus presentation and the pre- and the post-stimulus gray screen periods lasted 250 ms, and the number of trials was 10.

Input from Lateral Geniculate Nucleus (LGN)

Originally, the LGN spike trains used as input to the model were generated with the FilterNet module provided with the model, using 17,400 "LGN units" (Billeh et al., 2020). However, when this input was used for simulations, the onset of the evoked response in V1 was 20-30 ms delayed in comparison with experiments. Therefore, we used experimentally recorded LGN spike trains as input to the model instead. We assigned a recorded spike train to each of the 17,400 LGN units in all trials. In total, the public Neuropixels data contain recordings from 1,263 regular-spiking LGN neurons across 32 animals during 75 trials of full-field flash presentations. We divided the total pool of spike trains into 10 subsets, and then randomly sampled spike trains from one subset in each trial until all 17,400 LGN units had been assigned a spike train in all trials.

Input from lateromedial area (LM)

The experimentally recorded spike trains in the LM were used to construct the feedback input to V1. In total, the public Neuropixels data contain recordings from 1,823 regular-spiking LM neurons across 42 animals during presentations of the full-field flash stimulus. Spikes were randomly sampled from the pool of all spike trains to construct a spike train that was used as input to all the cells that were targeted by the feedback in the model. All neurons received the same spike train.

Background input

The input from the poisson source firing at 1kHz was not stimulus dependent. It is a coarse representation of the continuous influence of the rest of the brain on V1.

Dendritic targeting

LGN to V1

In the original model, the synapses from LGN onto excitatory V1 neurons were placed on apical and basal dendrites within 150 μm from the soma, while synapses onto inhibitory V1 neurons were placed on their soma and on their basal dendrites without distance limitations (Billeh et al. 2020). This placement was left unchanged in this study.

V1-V1

The synapses for recurrent connections were placed according to the following rules in the original model (Billeh et al. 2020):

<u>Excitatory-to-Excitatory Connections</u>

All synapses from excitatory V1 neurons onto other excitatory V1 neurons were placed along the dendrites and avoided the soma. In layers 2/3 and 4, the placement of synapses was restricted to be within 200 μm from the somata, while in layers 5 and 6, they could be placed anywhere along the dendrites.

Excitatory-to-Inhibitory Connections

All synapses from excitatory V1 neurons onto inhibitory V1 neurons were placed on their somata or dendrites without any distance limitations.

Inhibitory-to-Excitatory Connections

Synapses from Pvalb neurons onto excitatory V1 neurons were placed on the soma and on the dendrites within 50 μm from the soma. Synapses from Sst neurons were placed only on dendrites and only more than 50 μm from the soma. Synapses from Htr3a neurons were placed on dendrites between 50 and 300 μm from the soma.

Inhibitory-to-Inhibitory Connections

Synapses from inhibitory neurons to other inhibitory neurons were placed according to the same rules as the inhibitory-to-excitatory connections described above.

These placement rules were kept in this study, except for the synapses from excitatory neurons to excitatory L6 neurons. Here, they were restricted to be within 150 μm of the soma. The purpose of this restriction was to reduce the spatial separation between the current sink and source, and thereby decrease the magnitude of the L6 sink-source dipole.

LM-V1

The synapses from the node representing LM to V1 were placed on the apical dendrites of L2/3 neurons (within 150 μm from the soma), on the apical tufts (> 300 μm from the soma) and the basal dendrites (within 150 μm from the soma) of L5 excitatory cells, and on the somata and basal dendrites of L2/3 and L5 inhibitory cells (at any distance from the soma).

Adjusting synaptic weights

The synaptic weights for thalamocortical connections were left unchanged from the original model. Before the addition of feedback from higher visual areas to the model, the synaptic weights for recurrent connections in V1 were multiplied by factors in the range [0.2, 2.5]. After the addition of feedback, the synaptic weights from the background node to the populations targeted by feedback the L2/3 and L5 excitatory, Pvalb, and Sst cells were multiplied by factors in the range [0.2, 0.5]. The synaptic weights from the node representing

LM were initially set equal to the original weights between the background node and the populations targeted by the feedback, but this led to too high firing rates compared to the experimental firing rates in these populations, so they were multiplied by factors in the range [0.2, 0.5]. Finally, the connections from Pvalb neurons in V1 to L2/3 excitatory neurons and L5 excitatory cells were re-scaled in the range [0.8, 1.2] times the weights set prior to the addition of feedback.

Quantification and statistical analysis

Firing rates

The time-resolved population firing rates (bin size 1 ms, filtered using scipy.ndimage.gaussian_filter with sigma = 2) were computed by averaging the spike count over all cells in a population and over all trials (10 trials in the simulations and 75 trials in the experiments). The distribution of firing rates across cells used in the calculation of the KS-similarities were computed by averaging over the time windows baseline, initial peak, and sustained activity (defined in Fig. 3) and over all trials.

Kolmogorov-Smirnov similarity

The KS-similarity scores (Billeh et al., 2020) were computed by first calculating the KS-distance (using the function scipy.stats.ks_2samp) between two distributions of firing rates across cells, and subtracting this number from 1, such that a KS-similarity score of 1 implies identity and a score of 0 implies no overlap between the two distributions. In the comparison of the model to the experimental data, the KS-similarity was computed between the distribution of firing rates across cells in each RS and the FS population of the model and the distribution of firing rates across cells from all animals in the corresponding populations. To assess the variability in the experiments, the KS-similarity was calculated between the distribution of firing rates across cells in the same RS and FS populations in individual animals, provided there were more than 10 cells recorded in a given population in this animal, and the distribution of firing rates across cells from all other animals.

Correlation

We computed the similarity in the profile of time-resolved population firing rates with the Pearson correlation coefficient (using the function scipy.stats.pearsonr). The correlation between the model and the experimental firing rates was calculated between model population firing rates and the population firing rates averaged across cells from all animals. The level of experimental variability was assessed by calculating the correlation between

population firing rates in each animal and the population firing rates averaged across cells from all other animals.

CSD analysis

Since the number of recording electrodes in V1 are not the same in all animals, we interpolated the CSD of each animal and the CSD from simulations onto dimensions of the same lengths ($M = 30$ points along the depth and $K = 100$ points along the time axis for 100 ms time windows) before we quantitatively analyzed the CSD.

PCA

The trial-averaged CSD of each animal was flattened into a vector of length $M \times K = 3000$, and the vectors of all $N = 44$ animals were stacked together into a matrix of size 44×3000. Then, we performed PCA (using sklearn.decomposition.PCA) on this matrix to obtain the principal components which would constitute weighted averages of the trial-averaged CSD patterns.

Wasserstein distance (WD)

The 1st Wasserstein distance $W(P_1, P_2)$ between two distributions P_1 and P_2 is defined as

$$W(P_1, P_2) = \inf_{\gamma \in \Gamma(P_1, P_2)} \iint c(x, y)\gamma(x, y)dxdy$$

Where $c(x, y)$ is the cost of moving a unit "mass" from position x to y following the optimal transport plan $\gamma(x, y)$ in all transport plans $\Gamma(P_1, P_2)$ (Arjovsky et al., 2017; Rubner et al., 1998).

In the utilization of WD to quantify the similarity between two CSD patterns, the distance between the distribution of sinks in the two patterns $W(P_{sinks,1}, P_{sinks,2})$ and the distance between distribution of sources of the two patterns $W(P_{sources,1}, P_{sources,2})$ are calculated separately, and summed to form a total WD between the two CSD patterns:

$$W_{CSD}(P_1, P_2) = W(P_{sinks,1}, P_{sinks,2}) + W(P_{sources,1}, P_{sources,2})$$

where P_1 and P_2 refer to the two CSD patterns. The Python Optimal transport library (https://pythonot.github.io/index.html) was used to implement this calculation.

This application of the WD to compare CSD patterns comes with certain considerations that are important to note. First, although we compute WD for sinks and sources separately, sinks and sources do not arise independently. Current leaving the extracellular space in one place leads to current entering the extracellular space in another place, so current sinks and sources are inter-dependent. Second, the cost of shifting a sink or a source in space relative to shifting it in time is determined by the relative resolution in space vs. time. This relative cost does not necessarily correspond to the actual cost of changing the underlying physiology such that two distributions of sinks or sources match spatially vs. temporally. Determining the most appropriate relative cost of moving sinks and sources in space vs. time would require more detailed data than currently available and is beyond the scope of this study.

Code and data availability

The experimental data is publicly available at https://portal.brain-map.org/explore/circuits/visual-coding-neuropixels. The code and files necessary to run the model simulations presented here are available at https://www.dropbox.com/sh/x6zuogmjx8zns9f/AAAQbQbdXABsbbHUhC-qGBP7a?dl=0. The code for the data analysis performed in this paper is available at https://github.com/atleer/CINPLA_Allen_V1_analysis.git.